Mineralogy and chemical composition of ferromanganese crusts from the Cruzeiro do Sul Lineament - Rio Grande Rise, South Atlantic

Sousa I.M.C. [1, *], Santos R.V. [1], Koschinsky A. [2], Bau M. [2], Wegorzewski A.V. [3], Cavalcanti J.A.D. [4], Dantas E.L. [1]

[1] Instituto de Geociências, Universidade de Brasília, Campus Universitário Darcy Ribeiro, 70910-900, Brasília – DF, Brazil
[2] Department of Physics and Earth Sciences, Jacobs University Bremen, Campus Ring 1, 28759, Bremen, Germany
[3] BGR , Bundesanstalt für Geowissenschaften und Rohstoffe, Stilleweg 2, 30655, Hannover, Germany
[4] CPRM , Geological Survey of Brazil, Av. Brasil 1731, 30140-002, Belo Horizonte, MG, Brazil

* Corresponding author : I.M.C. Sousa, email address : isabela.sousa@unb.br

Abstract :

Samples dredged from the Cruzeiro do Sul Lineament exhibit ferromanganese crusts precipitated above phosphate-rich substrates (phosphorites, phosphate-impregnated volcanic rocks and older phosphatized ferromanganese crusts). Co-chronology of the crusts, paleontological data and 87Sr/86Sr ratios of the phosphatized substrate indicate that the last phosphatization event in the region happened between 17.6 and 14.6 Ma ago. When the event ceased, oxic conditions were resumed and hydrogenetic crust precipitation started at a maximum rate of 1.6–3.0 mm/Ma, forming layers of Fe-vernadite above the phosphorites. These crusts differ in composition from crusts that formed prior to the phosphatization, which were impregnated by carbonate fluorapatite and recrystallized forming a 10 Å Mn-phase, in expense of a lower crystallinity Mn-phase. Mn/Fe ratios of non-phosphatized crusts vary from 1.05 to 1.41. The Mn/Fe ratios as well as the metal content (Co = 0.65–1.04 wt%, Zn = 0.04–0.06 wt%, Cu = 0.02–0.06 wt% and Ni = 0.29–0.48 wt%) are similar to hydrogenetic crusts described in other parts of the world.

Highlights

► Non-phosphatized Fe–Mn crusts in the region developed above Miocene phosphorites. ► Phosphatization was probably caused by a Middle Miocene OMZ expansion in depth. ► Fe-vernadite is the mineral constituent of non-phosphatized Fe–Mn crusts. ► A stable 10 Å-Mn phase is the mineral constituent of phosphatized crusts. ► Estimated age of the crusts is in agreement with data from NE Atlantic.

Keywords : Rio Grande Rise, Ferromanganese crusts, Atlantic Ocean, Cruzeiro do Sul Lineament, Phosphatization

1. Introduction

Ferromanganese crusts and nodules are layered oxide-hydroxides precipitates from seawater that occur in all oceans over the world (Manheim & Lane-Bostwick, 1989; Hein et al., 1999). There has been an emerging interest about their resource potential for base and strategic metals, such as Co, Rare Earth Elements (REE) and platinum group elements (PGE), because of their possible use in high technology industries and clean energy purposes (Hein et al., 2013). Ferromanganese crusts are also regarded as condensed stratigraphic sections and have been studied to investigate changes in ocean chemistry (Christensen et al., 1997; Ling et al., 1997; Hein et al., 1999; Frank, 2011; Hein & Koshinsky, 2014).

Crusts grow over millions of years in areas of low terrigenous and biogenic sedimentation, where strong currents keep the substrate free from accumulating detrital/biogenic sediments (Hein & Koschinsky, 2014). Crusts concentrate metals from seawater by sorbing elements through strong coulombic interactions or incorporating them within the structure of iron and manganese oxide-hydroxides (Peacock and Sherman, 2007; Wegorzewski et al., 2020).

Hein et al. (1999) showed that the escarpments of seamounts are areas that commonly fulfill the requirements for crust formation. The Geologic Survey of Brazil (CPRM) organized four expeditions to study the geologic history of the Rio Grande Rise (Fig. 1) and investigate the occurrence of ferromanganese crusts on the escarpments of the Cruzeiro do Sul lineament.

In this study, petrographic, mineralogical and geochemical data as well as age estimates are presented to show that the Rio Grande Rise region has been favorable for hydrogenetic ferromanganese precipitation after a middle Miocene phosphatization event. These findings are interesting for revealing that the formation of phosphorites

52 and the ulterior ferromanganese precipitation is coeval with the youngest formation of

53 phosphorites in the Pacific Ocean and in the North Atlantic (Hein et al., 1993; Marino et

54 al., 2017).

55

56 **2. Regional Setting**

57 The Rio Grande Rise is a major topographic feature in the western South Atlantic

58 Ocean and occupies a conjugate position relative to the Walvis Ridge, located on the

59 African margin. At the summit of the rise, water depths are as shallow as 800 m, while

60 the surroundings are 4000 m deep (Fig. 1). The basement of the rise consists of a

61 Coniacian/Santonian tholeiitic basalt overlaid by late Cretaceous and Paleocene

62 sediments (Barker et al. 1981, Thompson et al., 1983; Rohde et al., 2013). Around 46

63 Ma ago, an alkaline magmatism uplifted and exposed the rise above sea level, resulting

64 in a hiatus of pelagic sedimentation (Fodor et al., 1980; Gamboa & Rabinowitz, 1984;

65 Rohde et al., 2013). After the Eocene, the rise subsided and pelagic sedimentation was

66 resumed. The rise is divided into an eastern (ERGR) and a western (WRGR) part. In

67 contrast to the WRGR, there are only limited data about the ERGR, which is a North-

68 South elongated feature built by an abandoned spreading center (Gamboa &

69 Rabinowitz, 1984). Both WRGR and ERGR are intercepted by the Cruzeiro do Sul

70 lineament, which is a 30-40 km wide valley trending NW-SE formed as an aborted rift

71 during the rearrangement of tectonic plates close to the Paleogene/Neogene boundary

72 (Mohriak et al., 2010; Galvão & de Castro, 2017).

73

74 **3. Sample collection**

75 Samples were collected during legs 1 to 4 of the *Geological and Geophysical*

76 *Expedition to International Waters of the South Atlantic*, carried out by the Geological

77 Survey of Brazil (CPRM). Legs were held aboard *R/V Marion Dufresne* between June

78 and July of 2011. Hundreds of dredging stations were investigated at both WRGR and

79 ERGR, and ferromanganese crust samples described in this study are from 13 different

80 sites along the slopes of Cruzeiro do Sul Lineament (Table 1, Fig. 2). A total of 14

81 samples were selected among rocks of the dredging stations for chemical

82 characterization and two samples were selected for $^{87}Sr/^{86}Sr$ measurements.

83

84 **4. Methods**

85 4.1 Petrography, Micropaleontology and Electron Probe Micro-analyzer (EPMA)

86 Thin sections of the crusts and their substrates were studied under a petrographic

87 microscope for microfossil and mineral identification. Foraminifera were identified in

88 thin sections to the genus level, when possible. Taxonomy of foraminifera specimens

89 was mainly in reference to Blow (1979), Kennett & Srinivasan (1983) Loeblich &

90 Tappan (1987) and BouDagher-Fadel (2008). Quantitative spot analyses (Wavelength-

91 Dispersive X-ray Spectrometry - WDS) of micrometric layers on the ferromanganese

92 crust of sample ML77A was performed in a JEOL JXA 8230 EPMA. Spot analyses

93 were also performed on the substrate of samples ML77A, DC38A, DC25A and DC61B

94 to investigate the composition of the matrix. Analyses were performed using 15 kV

95 voltage, 10 nA current and a spot size beam of 5 μm. Counting time for all elements

96 was 10 seconds in the peak, and 5 seconds in upper and lower background positions.

97 Analyses were performed at the Electron Microprobe Lab at the University of Brasília.

98

99   4.2 Inductively Coupled Plasma Optical Emission Spectrometry (ICP-OES) and

100 Inductively Coupled Plasma Mass Spectrometry (ICP-MS)

101 Major and trace elements of the ferromanganese crusts were analyzed at Jacobs

102 University Bremen (JUB), Germany, by ICP-OES and ICP-MS. All samples were

103 carefully separated from their substrate, powdered in an agate pan mill and dried at

104 105°C for 24 h. Immediately after drying, 0.05 mg of each sample was digested with

105 HCl, HNO_3 and HF in a ratio of 3:1:1 ml. Samples in the acid mixture were heated to

106 225°C for 12 hours in closed vessels that were later opened and kept at 180°C for acid

107 evaporation. Digested samples were stored in 0.5 M HNO_3 and 0.05 M HCl. Samples

108 were diluted 3.000 times for Mn, Fe, Cu, Al, K, Ca, Mg, Na, P, V and Zn measurement

109 using Spectro Ciros Vision (ICP-OES). Determination of Li, Sc, Ti, Co, Ni, Rb, Sr, Y,

110 Zr, Nb, Mo, Te, Cs, Ba, REE, Hf, Ta, W, Pt, Pb, Th and U was performed in NEX ION

111 350X (ICP-MS), in samples 100.000 times diluted. Certified standard material JMn-1

112 (Ferromanganese nodule from the Geological Survey of Japan) was used for precision

113 and accuracy determination. Detailed description of the methodology, accuracy,

114 precision and interference are in Alexander (2008).

115

116 4.3 X-ray diffractometry (XRD)

117 Mineralogy of the bulk samples was determined using PANalytical X'Pert PRO MPD

118 θ-θ diffractometer (Cu-Kα radiation), with 40 kV and 40 mA at the German Federal

119 Institute for Geosciences and Natural Resources (BGR), in Hannover. The

120 diffractometer is equipped with a variable divergence slit (20 mm irradiated length) and

121 a Scientific X'Celerator detector (active length 2.122°; phd 60). Samples were scanned

122   over 5° to 85° 2 θ with a step size of 0.0334° 2 θ and a measuring time of 200 sec/step.

123   Afterwards, data were processed using the software *High Score Plus*.

124   Samples in which a 10 Å manganese phase was identified in a first analysis underwent a

125   heating treatment (105°C for 48 hours) in order to distinguish 10 Å todorokite from 10

126   Å phyllomanganate. Heating promotes changes in the stacking order of

127   phyllomanganates, but does not affect todorokite (Uspenskaya et al., 1987;

128   Wegorzewski et al., 2015). This happens because upon drying at 105 °C,

129   phyllomanganates lose interlayered water, leading to a collapse of the interlayer and,

130   consequently, to a decrease of the layer-to-layer distance from 10 Å to 7 Å (Uspenskaya

131   et al., 1987).

132

133   4.4 ^{87}Sr/^{86}Sr ratio measurement

134   ^{87}Sr/^{86}Sr ratios of the substrate on ferromanganese sample HS-145a and on a carbonate

135   vein in sample ML11D were determined through TIMS (Thermal Ionization Mass

136   Spectrometry), in a Finningan MAT 262 at the University of Brasília. Samples were

137   digested in H_3PO_4 and the residue kept in a HNO_3 (2.9 N) solution for column

138   chromatography. The solution containing Sr was collected, dried and then dissolved in 1

139   ml HNO_3 (50%) for analysis. Procedures followed steps used by Alvarenga et al.

140   (2007). NBS-987 was used as reference material, and yielded a ^{87}Sr/^{86}Sr ratio of

141   0.71028 ± 1 (1σ).

142

143 **5. Results**

144 5.1 Morphology of the samples

145 Through visual description we identified pristine ferromanganese crusts layers (not

146 impregnated with light colored minerals such as phosphates and carbonates), and

147 phosphatized ferromanganese crusts. Pristine samples are laminated or botryoidal and

148 occur in sharp contact above phosphorites (Fig. 3A, 3C, 3D, 3E), volcanic rocks (Fig.

149 3B) or above an older phosphatized crust (Fig. 3G). Phosphatized samples tend to be

150 massive and dense, without clear visible laminae (Fig. 3F, 3G). In phosphatized

151 samples, it is not possible to identify a sharp contact between the dark ferromanganese

152 layers and the substrate because orange and yellowish phosphate aggregates occur

153 within the ferromanganese crust. A summary of crust characteristics is presented in

154 Table 2 and Fig. 3. In Fig. 3A, sample ML77A exhibits a 16 mm-thick non-

155 phosphatized crust developed around an orange lithified phosphorite. Sample DC61B

156 exhibits a thin crust (6 mm) precipitated above a vesicular volcanic rock (Fig. 3B). In

157 Fig. 3C, sample DC38A shows a 25 mm-thick non-phosphatized crust with botryoidal

158 texture developed above a white/yellowish lithified phosphorite. Figure 3D shows a 20

159 mm-thick laminated ferromanganese crust above a brownish lithified phosphorite

160 (sample DC25C). Figure 3E shows a 20 mm-thick laminated crust above a phosphorite.

161 Figure 3F shows sample DC25A, which is a mixture of ferromanganese minerals and

162 phosphate. The surface of sample DC25A exhibits botryoidal texture, and only the

163 outermost layer (1 mm) lacks phosphate stains. Figure 3G shows a 6 mm-thick crust,

164 with laminated texture, developed above an older and phosphatized crust that contains

165 orange phosphate stains (ML67B). This sample had the non-phosphatized part (the

166 upper 6 mm, ML67B-2) and the phosphatized part analyzed (ML67B-1).

167

168   5.2 Petrography and EPMA results of the crusts

169   Ferromanganese crusts are opaque to transmitted light and therefore were better

170   observed through electron imaging (Fig. 4). The micrometric layers of the crusts present

171   concave structures (Fig. 4A) of slightly different reflectance (backscattered-electrons

172   image). The sum (wt.%) of iron, manganese, cobalt, zinc, copper and nickel is lower in

173   darker layers than in lighter layers (Table 3). Figure 4B shows the contact between the

174   crust and its underlying phosphorite (substrate).

175

176   5.3 Micropaleontology and EPMA results of the substrate

177   The identification of foraminifera genus was performed in thin sections and focused on

178   providing age constraints for the samples (Table 4). In the substrate of sample ML77A

179   it was possible to identify *Discocyclina sp.*, *Nummulites sp.* (Fig. 5B) and calcareous

180   structures produced by coralline algae within the phosphatized part, and *Orbulina sp.*

181   was observed in the non-phosphatized part of the substrate. In sample DC38A (Fig.

182   6A), *Orbulina sp.* occurs within the phosphorite substrate (Fig. 6B) of the crust, and in

183   the substrate of sample DC25A, we recognized *Morozovella sp.* (Fig. 6D),

184   Yellow dots shown in Fig. 5 and Fig. 6 are EPMA spot analyses reported in Table 5.

185   EPMA results reveal high phosphorus contents in the substrate of all samples (>4 %),

186   except in the white fragment of the substrate in sample ML77A, that is composed of

187   calcium carbonate. Among the samples studied in this paper, sample DC61B is the only

188   one that has a volcanic substrate. EPMA analysis on the vesicular glassy matrix also

189   shows a high phosphorus content.

190

191 5.4 Mineralogy of bulk samples

192 XRD data revealed that non-phosphatized layers of the samples are composed of Fe-

193 vernadite (δ-MnO$_2$; Fig. 7), which is characterized by two hk0 reflections (2.45 (01) Å

194 and 1.45 Å (11)) and no stacking of layers in the crystallographic c* direction. Calcite

195 and quartz may be present to a lesser extent.

196 Older phosphatized samples are composed of a stable 10 Å Mn-phase instead of a Fe-

197 vernadite. Being stable means that the mineral remains unaffected after a heating

198 treatment at 105°C for 48 hours (Fig.8). The heating procedure was carried out to

199 evaluate whether the mineral loses the 10 Å peak, such as phyllomanganates, or not,

200 such as todorokite (Uspenskaya et al., 1987). After the heating procedure, the 10 Å

201 reflex remains stable, which indicates it is todorokite. However, the todorokite

202 reflection at 2.39 Å is missing. In addition, the 10 Å peak does not have the sharpness

203 nor the intensity expected for todorokite under the same analytical conditions. For this

204 reason, we opted for calling this mineral a stable 10 Å Mn phase, instead of todorokite.

205 Carbonate fluorapatite (CFA) and calcite are present in all phosphatized samples.

206

207 5.5 Bulk geochemistry

208 Bulk chemical composition of the 14 analyzed samples is presented in Table 6. Non-

209 phosphatized samples are mainly composed of Fe (17-21 wt.%) and Mn (20-25%),

210 while phosphatized samples have lower Fe (10-19 wt.%) and Mn (6-12 wt.%) contents.

211 Phosphatized samples are enriched in P (>1.5 wt.%) and Ca (>11.54% wt.%), when

212 compared to non-phosphatized samples (Fig. 9), which have low Ca (<3.4 wt.%) and P

213 (<0.56 wt.%). Sample DC25C is not phosphatized, but its higher Ca content can be

214 explained by the presence of calcite, not visible in hand sample, but evident in XRD

215 results.

216 Differences in the composition of the substrate and morphology of the crusts do not

217 affect the chemical composition. Figure 9 compares the Mn/Fe ratio and the

218 concentration of selected elements for both phosphatized and non-phosphatized

219 samples. In non-phosphatized samples the Co contents range from 0.65 to 1.04 wt.%. In

220 phosphatized samples the Co contents are much lower (0.20-0.52 wt.%). Zn (0.04-0.06

221 wt.%), Cu (0.02-0.05 wt.%) and Ni (0.26-0.62 wt.%) do not have a significant variation

222 between phosphatized and non-phosphatized samples.

223 In the REE spidergram, Y is inserted between Dy and Ho (Fig. 10), based on its ionic

224 radius (Bau & Dulski, 1995), to allow better comparison with its geochemical twin Ho.

225 Post-Archean Australian Shale (McLennan, 1989) normalized REY patterns show a flat

226 pattern for the samples, with pronounced positive Ce anomaly and negative Y anomaly.

227 Phosphatized crusts have an overall lower content of REE than phosphatized crusts,

228 lower Ce anomaly and a positive Y anomaly. REE contents range between 2167 and

229 2841 ppm in non-phosphatized crusts, and between 675 and 1576 ppm in phosphatized

230 crusts.

231 5.6 Cobalt chronology and growth rates

232 Growth rate and age estimates were calculated based on Co concentration of the non-

233 phosphatized samples, following the equation proposed by Puteanus & Halbach (1988):

234 G.R.=1,28/[Co(%)-0,24]. The Co flux into ferromanganese crusts is considered to be

235 constant over the entire growth period of the samples (Puteanus & Halbach, 1988).

236 Thus, the growth rate is correlated to the Co enrichment in each layer. Thus, the higher

237 the growth rate the lower the Co concentration. Co chronometry is an empirical method

238 that matches isotopic determinations, but is unable to measure possible hiatuses during

239 accretion. Hence, growth rates represent maximum values and ages correspond to

240 minimum values. This equation has been used for the past thirty years and has been

241 proven to provide consistent age estimates by different authors (Josso et al., 2019; Yi et

242 al., 2020).

243 Non-phosphatized samples from the Rio Grande Rise yielded ages between 5 and 16

244 Ma (Table 6), with growth rates ranging from 1.6 to 3.0 mm/Ma. Co chronometry

245 measurements were performed using the whole thickness of the crusts in all non-

246 phosphatized samples.

247 5.7 ^{87}Sr/^{86}Sr indirect dating

248 ^{87}Sr/^{86}Sr analyses on a carbonate vein from sample ML11-D and on the phosphatized

249 substrate of sample HS145a yielded ratios of 0.70860+/-2 and 0.70880+/-2 (Fig. 11;

250 Table 7). Comparing the ^{87}Sr/^{86}Sr ratio of the samples to the curve of the Sr isotope

251 composition of the oceans through the Cenozoic (McArthur et al., 2012), we suggest

252 that analyzed materials crystalized at 17.6 and 14.6 Ma ago, respectively (Fig. 12).

253 These Sr isotope ratios represent isotope ratios without an age correction to subtract

254 radiogenic ^{87}Sr produced by internal decay of ^{87}Rb after the time of deposition.

255 Phosphate minerals and calcite have a low ^{87}Rb/^{86}Sr ratio (<0.01) with a high

256 concentration of unradiogenic Sr (Faure & Powell., 1972; Faure, 2001). Thus, the age

257 correction is almost negligible for the Sr isotope. However, data must be interpreted

258 with care because Sr ages of carbonate and carbonate fluorapatite are susceptible to

259 diagenetic effects: incorporation of Sr during the crystallization of authigenic minerals

260 might drive ages to younger values, but since Co chronology and paleontological data

261 corroborate ^{87}Sr/^{86}Sr dating, we suggest that diagenetic effects are negligible in our

262 samples.

263 **6. Discussion**

264 6.1 Mineralogy of the crusts

265   The mineralogy of non-phosphatized samples is dominated by Fe-bearing vernadite (δ-

266   MnO_2), possibly intergrown with amorphous iron oxyhydroxide (δ-FeOOH)

267   nanoparticles (Koschinsky et al., 2010). This is typical of seawater-sourced precipitates

268   that formed under oxic conditions. In phosphatized samples the Mn-phase is the initial

269   transformation from a layered manganate into a tunnel structure, but without a perfect

270   3x3 octahedra tunnel structure. It probably corresponds to a distorted structure of

271   todorokite, transitioning from very low crystallinity Fe-vernadite. This phase has both

272   10 Å and 4.8 Å reflections, but lacks the characteristic 2.39 Å reflex of todorokite.

273   Instead, it has the typical peaks of phyllomanganates (vernadite, 2.44 Å and 1.42 Å).

274   The Mg contents in these samples (1.85 – 1.97 wt.%) is lower than expected for

275   minerals diagenetically transitioning to todorokite (Manceau et al., 2014), which have

276   around 4 wt.% of Mg. Therefore, the manganate of phosphatized samples will be

277   reported as stable 10 Å Mn-phase, and not as typical todorokite. This 10 Å-Mn phase

278   shows high amounts of incorporated Zn, Cu and Ni, but low Co contents, which is

279   characteristic for suboxic enrichment (Manceau et al., 2014) and was also reported by

280   Koshinsky et al. (1997) in phosphatized samples. In vernadite, Mn occurs in oxidation

281   state +4, while 10Å-Mn oxides contain Mn of less oxidated states, which also

282   demonstrates the suboxic character of the environment in which the 10Å-Mn phase

283   crystallized.

284

285   6.2 Classification and age of crusts

286   Ferromanganese crusts precipitated above phosphorites plot within the hydrogenetic

287   field of the ternary diagram Fe-Mn-10*(Ni+Cu+Co) (Fig.13; Bonatti et al., 1972). They

288   also plot within the hydrogenetic fields of Y_{SN}/Ho_{SN} vs $Ce_{SN}/Ce_{SN}*$ and Nd vs

289    $Ce_{SN}/Ce_{SN}*$ diagrams (Fig. 14) proposed by Bau et al. (2014). These diagrams are not

290 appropriate to classify phosphatized samples because their chemical composition was

291 altered during phosphatization.

292 Considering (i) the presence of *Orbulina sp.* (Kennett & Srinivasan, 1983) on the

293 phosphorites, which first occurrence was 15.1 Ma ago; (ii) the indirect dating of the

294 substrate through $^{87}Sr/^{86}Sr$ ratios (14.6-17.6 Ma); and (iii) the age of the ferromanganese

295 crusts calculated with Co chronology (5-16 Ma), we suggest that the phosphatization

296 event occurred between 14.6 and 17.6 Ma ago and once it ceased, crust precipitation

297 was resumed. These ages are in agreement with ages reported by González et al. (2016)

298 for the last phosphatization event in the Galicia Bank, NE Atlantic (18.5 – 17.7 Ma).

299 The presence of the 10Å Mn-phase in older crusts can be explained by the

300 recrystallization of a less ordered manganate phase during the phosphatization. The

301 event of phosphatization also caused the impregnation of preexisting sediments with

302 carbonate fluorapatite and possibly was a period of no crust precipitation, due to the

303 suboxic condition of phosphate-rich waters.

304 The estimated ages of the crusts are in agreement with ages reported by Benites et al.

305 (2020), who studied ferromanganese crusts from the summit of the Rio Grande Rise. In

306 a sample from the São Paulo Plateau (Fig. 1), located 500 km eastwards from the Rio

307 Grande Rise and at a 2781 m water depth, Goto et al. (2017) suggested favorable

308 environmental conditions for crust precipitation during the last 30 Ma. However,

309 different from the Rio Grande Rise, there is no evidence of phosphatization during the

310 growth interval of the studied sample. In another sample from the São Paulo Plateau,

311 Nozaki et al. (2017) dated the base of a ferromanganese crust at ca. 5 Ma.

312

313 6.3 The REY composition of the crusts

314   The positive Ce anomaly is common in hydrogenetic ferromanganese crusts, because

315   Ce is redox-sensitive and oxidizes after sorption at the oxyhydroxide surface from

316   dissolved Ce(III) to insoluble Ce(IV) (Bau et al., 1996; Bau & Koschinsky, 2009).

317   The phosphatization process occurs under sub-oxic conditions, Ce is reduced and

318   remobilized. Thus, phosphatized samples do not have positive Ce anomalies of the same

319   extent as non-phosphatized samples. In non-phosphatized samples, the calculated Ce

320   anomaly $Ce_{SN}/Ce_{SN}^*=Ce_{SN}/(0.5La_{SN}+0.5Pr_{SN})$ varies from 2.3 to 3.4, while in non-

321   phosphatized crusts values drop to 1.7-3.0.

322   The negative Y anomaly of non-phosphatized crusts is not controlled by the redox state,

323   but by the strength of surface complexes (Bau & Dulski, 1994). Ho and Dy form

324   stronger surface-complexes than Y on ferromanganese precipitates. Thus, as the surface

325   complex of Y is less stable, there is a decoupling of Y and Ho that drives negative Y

326   anomalies in the REY pattern (Bau & Dulski, 1994; Bau et al, 1996). In contrast,

327   phosphatized samples have a positive Y anomaly because the impregnation of

328   phosphate in the pores of ferromanganese crusts imprints a seawater-like composition to

329   the samples. The positive Y anomaly in phosphatized crusts is caused by the

330   introduction of Y during the crystallization of stable phosphate phases (Koschinsky et

331   al., 1997). The calculated negative Y anomaly $Y_{SN}/Y_{SN}^*=Y_{SN}/(0.5Dy_{SN}+0.5Ho_{SN})$ is

332   0.5-0.9 in non-phosphatized and 0.9-1.4 in phosphatized samples.

333   Figure 15 exhibits Ce_{SN}/Ce_{SN}^* vs La_{SN}/Lu_{SN} graphic, where the difference in REE

334   behavior between phosphatized crusts and non-phosphatized crusts is shown. Carbonate

335   fluorapatite is more enriched in MREE and HREE than Fe-Mn oxides, as a result

336   La_{SN}/Lu_{SN} ratio of phosphatized samples is lower than the ratio of non-phosphatized

337   samples.

338

339   6.4 Aspects of subsidence and ocean circulation

340   The presence of photosynthetic algae structures (Coralline algae) and large benthic

341   foraminifera specimens (*Discocyclina sp.* and *Nummulites sp.)* in the phosphatized

342   substrate of sample ML77A indicates an Eocene age for the assemblage and it is

343   characteristic of shallow waters. These data evidence the Eocene uplift of the rise

344   (Gamboa & Rabinowitz, 1984). Younger assemblages in which *Orbulina sp.* occurs are

345   dominated by planktic foraminifera and lack photosynthetic specimens, indicating

346   greater water depths since the Miocene.

347   The Zr/Hf ratio (Schmidt et al., 2014) as well as Y/Ho ratio (Bau et al., 1995; Censi et

348   al., 2007) are interesting tracers of water masses. Crusts from the Pacific Ocean were

349   expected to have higher Zr/Hf and Y/Ho ratios than crusts from the Atlantic, because Hf

350   and Ho have a particle reactive behavior and are preferentially removed from the water

351   through the ocean conveyor belt, with respect to their geochemical twin. However, only

352   Zr/Hf ratios behave as expected (Fig. 16), while Y/Ho values are very similar in

353   Atlantic and Pacific samples. Thus, we suggest that the higher Zr/Hf ratios of Pacific

354   crusts are a consequence of Hf removal through time during ocean circulation. Rickli et

355   al. (2009) suggest Hf is preferentially removed from seawater by adsoption on biogenic

356   opal. The interaction with opal rich waters (e.g. Southern Ocean) on the Strait of

357   Magellan could be one possible explanation for the difference in Zr/Hf ratios of samples

358   from the two oceans. Y/Ho ratios are very similar in Pacific and Atlantic crust samples

359   possibly because the weak complexation of Y is a ubiquitous feature in ferromanganese

360   crusts that overprints a possible effect of different water masses.

361

362   6.4 Comparison with ferromanganese crusts from Northeast Atlantic

363   Ferromanganese crusts from the Canary Islands, on the East Atlantic, present

364   anomalous contents of Fe and Al, due to their proximity to the continental crust, eolian

365   input and authigenic formation of phyllosilicates (Hein et al., 2000; Marino et al.,

366   2017). This is not observed in crusts from the Rio Grande Rise, because they

367   precipitated far enough from the continent. However, the formation of crusts in both

368   areas of the Atlantic is coeval and a phosphatization event is also recorded by samples

369   from the Canary Islands (Marino et al., 2017). Koschisnky et al. (1996) investigated

370   ferromanganese samples from other two seamounts in the Northeast Atlantic (Lion and

371   Tropical seamounts), and show that the age of the crusts in these seamounts is very

372   similar to ages estimated in this paper (ca. 12 Ma), but the phosphatization event dated

373   by Koschinsky et al. (1996) might be as old as 30-40 Ma.

374

375   6.5 Causes of phosphatization

376   The phosphatization of ferromanganese crusts and the formation of phosphorites on

377   seamounts is generally associated with changes in climatic conditions and with the

378   spreading of phosphate-rich sub-oxic waters throughout the ocean (Halbach et al., 1982,

379   1989; Hein et al., 1993; Hyeong et al., 2013). Halbach et al. (1982, 1989) proposed that

380   the phosphatization on seamounts is caused by the expansion of oxygen minimum zones

381   (OMZ) as a result of increased productivity in surface waters. This process would have

382   expanded the limits of OMZ at depth, making it reach the top of seamounts and

383   impregnating sediments with phosphorous. Kraal et al. (2012) show that in the Arabian

384   Sea, authigenic formation of calcium-phosphate minerals occurs where the OMZ

385   intersects the seafloor topography. However, they also show that a large fraction of

386   phosphates is not authigenic and was deposited from the water column.

387 Other authors suggest that phosphorus-rich waters may have accumulated in deep areas

388 of the ocean during periods of sluggish circulation, and later, during normal circulation

389 conditions, upwelled on the edge of seamounts (Hein et al., 1993).

390 Our data do not allow constraining further details about the source of the phosphorous-

391 rich waters that caused the phosphogenesis in the RGR. However, comparing our

392 samples to the sample from the São Paulo Plateau (Goto et al., 2017), we observed that

393 all our crusts are either phosphatized or precipitated above a phosphorite and are from

394 shallower sites (688-1798 m) than the sample from the São Paulo Plateau (2871 m), that

395 is not phosphatized. Thus, we suggest that the expanded OMZ is most likely the source

396 of phosphorous. We do not discard the hypothesis that this event overprinted multiple

397 phosphatization events that happened prior to the Miocene.

398 **7. Summary and conclusions**

399 Ferromanganese crusts that precipitated above phosphate-rich substrates (phosphorites,

400 phosphate-impregnated volcanic rocks and older phosphatized ferromanganese crusts)

401 on the Rio Grande Rise grew after a middle Miocene phosphatization event that was

402 responsible for recrystallizing older crusts and impregnating sediments with carbonate

403 fluorapatite.

404 Crusts that formed after the phosphatization are composed of Fe-vernadite, which is a

405 phyllomanganate, typical of hydrogenetic precipitates under oxic conditions. Instead of

406 vernadite, older crusts affected by the phosphatization have a stable 10 Å Mn-phase,

407 which is a product of recrystallization of a less ordered Mn-phase under sub-oxic

408 conditions during the phosphatization event.

409 All non-phosphatized crusts yielded Co chronometric minimum ages between 5 and 16

410 Ma, with maximum growth rates ranging from 1.6 to 3.0 mm/Ma. Marino et al. (2017)

411 showed that ferromanganese crusts from the Northeast Atlantic Ocean were also

412 affected by phosphatization in the Miocene. Applying more precise dating methods in

413 the crusts and their substrates will allow better interpretations regarding the

414 paleoceanography through the Neogene-Quaternary in the region, and may provide

415 insightful data on Miocene ocean chemistry and its response to climate changes.

416

Acknowledgments

References

424 Alexander, B., 2008. Trace element analyses in geological materials using low resolution ICPMS. Jacobs University
425 Technical Reports, 18, 1–78. Available at: http://nbn-resolving.org/urn:nbn:de:gbv:579-opus-1006789.

426 Alvarenga, C.J.S., Della Giustina, M.E.S., Santos, R.V., Gioia, S., Guimarães, E.M., Dardenne, M.A., 2007.
427 Variações dos isótopos de C e Sr em carbonatos pré e pós-glaciação Jequitaí (Esturtiano) na região de Bezerra-
428 Formosa, Goiás. Revista Brasileira de Geociências, 37, 999-1007.

429 Barker P.F., Carlson R.L., Johnson, D.A., Cepek, P., Coulbourn, W.,Gamboa, L.A., Hamilton, N., Melo, U., Pujol,
430 C., Shor, A.N., Suzyumov, A.E., Tjalsma, L.R.C., Walton, W.H., Weiss, W., 1981. Deep Sea Drilling Project Leg 72:
431 Southwest Atlantic paleocirculation and Rio Grande Rise tectonics. Geological Society of America Bulletin, 92, 294-
432 309.

433 Bau, M., Koschinsky, A., Dulski, P., Hein, J.R., 1996. Comparison of the partitioning behaviours of yttrium, rare
434 earth elements, and titanium between hydrogenetic marine ferromanganese crusts and seawater. Geochimica et
435 Cosmochimica Acta, 60(10), 1709–1725.

436 Bau, M., Dulski, P., 1995. Comparative study of yttrium and rare-earth element behaviours in fluorine-rich
437 hydrothermal fluids. Contributions to Mineralogy and Petrology, 119, 213-223.

438 Bau M., Dulski P., Môller, P., 1995. Yttrium and holmium in South Pacific seawater: Vertical distribution and
439 possible fractionation mechanisms. Chemie der Erde, 55, 1-15.

440 Bau, M., Dulski, P., 1994. Evolution of the yttrium-holmium systematics of seawater through time. Mineralogical
441 Magazine - Goldschmidt Conference Abstracts, 58A, 61-62.

442   Bau, M., 1996. Controls on the fractionation of isovalent trace elements in magmatic and aqueous systems: evidence
443   from Y/Ho, Zr/Hf, and lanthanide tetrad effect. Contributions to Mineralogy and Petrology, 123, 323–333

444   Bau, M., Koschinsky, A., 2009. Oxidative scavenging of cerium on hydrous Fe oxide: Evidence from the distribution
445   of rare earth elements and yttrium between Fe oxides and Mn oxides in hydrogenetic ferromanganese crusts.
446   Geochemical Journal., 43(1), 37–47.

447   Bau, M., Schmidt, K., Hein, J.R., Kuhn, T., Usui, A., 2014. Discriminating between different genetic types of marine
448   ferro-manganese crusts and nodules based on rare earth elements and yttrium. Chemical Geology, 381, 1–9.
449   Available at: http://dx.doi.org/10.1016/j.chemgeo.2014.05.004.

450   Benites, M., Hein, J.R., Mizell, K., Blackburn, T., Jovane, L., 2020. Genesis and Evolution of Ferromanganese Crusts
451   from the Summit of Rio Grande Rise, Southwest Atlantic Ocean. Minerals, 10, 349.

452   Blow, W.H., The Cainozoic Globigerinida., 1979. E.J. Brill, Leiden.

453   Bonatti, E., Kraemer, T., Rydell, H., 1972. Classification and genesis of submarine ironmanganese deposits. In: Horn,
454   D.R. (Ed.), Ferromanganese Deposits of the Ocean Floor. Arden House, New York, 149–165.

455   BouDagher-Fadel, M.K. Evolution and Geological Significance of Larger Benthic Foraminifera., 2008. UCL Press,
456   London.

457   Censi, P., Zuddas, P., Larocca, D., Saiano, F., Placenti, F., Bonanno, A., 2007. Recognition of water masses
458   according to geochemical signatures in the Central Mediterranean sea: Y/Ho ratio and rare earth element behavior.
459   Chemistry and Ecology, 23(2), 139-155.

460   Christensen, J.N., Halliday, A.N., Godfrey, L.V., Hein, J.R., Rea, D.K., 1997. Climate and ocean dynamics and the
461   lead isotopic records in Pacific ferromanganese crusts. Science, 277, 913.

462   Constantino, R.R., Hackspacher, P.C., de Souza, I.A., Costa, I.S.L., 2017. Basement structures over Rio Grande Rise
463   from gravity inversion. J. S. Am. Earth Sci., 75, 85–91.

464   Faure, G., 2001. Origin of Igneous Rocks - The Isotopic Evidence. Springer-Verlag, Heidelberg. 496 pp.

465   Faure, G., Powell, J.L., 1972. Strontium Isotope Geology. 188 pp. Springer-Verlag, Berlin, Heidelberg, New York.

466   Flower, B.P., Kennett, J.P., 1994. The middle Miocene climatic transition: East Antarctic ice sheet development,
467   deep ocean circulation and global carbon cycling. Palaeogeogr. Palaeoclimatol. Palaeoecol., 108(3–4):537–555.
468   https://doi.org/10.1016/0031-0182(94)90251-8

469   Fodor, R.V., Kumar, N., Bornhorst, T.J., Husler, J.W., 1980. Petrology of basaltic rocks from the São Paulo ridge,
470   southwestern Atlantic Ocean. Mar. Geol., 36(1-2), 127-141.

471   Frank M. 2011. Oceanography: chemical twins, separated. Nat. Geosci. 4, 220–221.

472   Futa, K., Peterman, Z.E., Hein, J.R., 1988. Sr and Nd isotope variations in ferromanganese crust from the Central
473   Pacific: implications for age and source provenance, Geochimica et Cosmochimica Acta, 52, 2229–2233.

474   Galvão, I.L.G. de Castro, D.L., 2017. Contribution of global potential field data to the tectonic reconstruction of the
475   Rio Grande Rise in the South Atlantic. Marine and Petroleum Geology, 86, 932-949.

476   Gamboa, L.A.P., Rabinowitz, P.D., 1984. The evolution of the Rio Grande Rise in the southwest Atlantic Ocean.
477   Mar. Geol., 58(1–2), 35–58.

478   Gioia, S.M.C.L., Pimentel, M.M., 2000. The Sm-Nd isotopic method in the geochronology laboratory of the
479   University of Brasília. An. Acad. Bras. Ciênc., 72(2), 219-245.

19

480 Glasby, G.P. Manganese: predominant role of nodules and crusts. In: Schulz, H.D., Zabel, M. (Eds.). Marine
481 Geochemistry. Springer-Verlag, Berlin Heidelberg, 2006. 371-427.

482 González, F.J., Somoza, L., Hein, J.R., Medialdea, T., León, R., Urgorri, V., Reyes, J., Martín-Rubí, J.A., 2016.
483 Phosphorites, Co-rich Mn nodules, and Fe-Mn crusts from Galicia Bank, NE Atlantic: reflections of Cenozoic
484 tectonics and paleoceanography. Geochem.Geophys. Geosyst. 17. http://dx.doi.org/10.1002/2015GC005861.

485 Goto, K.T., Nozaki, T., Toyofuku, T., Augustin, A.H., Shimoda, G., Chang Q., Kimura, J.I., Kameo, K., Kitazato, H.,
486 Suzuki, K., 2017. Paleoceanographic conditions on the São Paulo Ridge, SW Atlantic Ocean, for the past 30 million
487 years inferred from Os and Pb isotopes of a hydrogenous ferromanganese crust. Deep-Sea Research Part II: Topical
488 Studies in Oceanography, 146, 82–92.

489 Grau, R., Kudrass, H.R., 1991. Pre-Eocene and younger manganese crusts from the Manihiki Plateau, southwest
490 Pacific Ocean. Mar. Mining., 10, 231-246.

491 Halbach, P., Manheim, F.T., Otten, P., 1982. Co-rich ferromanganese deposits in the marginal seamount regions of
492 the central Pacific basin – results of the Midpac '81. Erzmetall., 35, 447-453.

493 Halbach, P., Sattler, C.D., Teichmann, F., Washner, M., 1989. Cobalt-rich and platinum-bearing manganese crust
494 deposits on seamounts: nature, formation, and metal potential. Mar. Mining, 8, 23-39.

495 Halbach, P., Kriete, C., Pause, B., Puteanus, D., 1989. Mechanisms to explain the platinum concentration in
496 ferromanganese seamount crusts. Chemical Geology, 76 (1-2), 96-106.

497 Hein, J.R., Koschinsky, A., Bau, M., Manheim, F.T., Kang, J.-K., Roberts, L. Cobalt-Rich Ferromanganese Crusts in
498 the Pacific. In: Cronan, D.S. (Ed.). Handbook of Marine Mineral Deposits. CRC Press, Boca Raton, FL. 1999. 239-
499 281.

500 Hein, J.R., Koschinsky, A., 2014. Deep-ocean ferromanganese nodules and crusts. In: Holland, H.D., Turekian, K.K.
501 (Eds.), Treatise on Geochemistry. 2nd Edition. Elsevier, Oxford, pp. 273-291.

502 Hein, J.R., Koschinsky, A., Halliday, A.N., 2003. Global occurrence of tellurium-rich ferromanganese crusts and a
503 model for the enrichment of tellurium. Geochimica et Cosmochimica Acta, 67(6), 1117–1127.

504 Hein, J.R., Mizell, K., Koschinsky, A., Conrad, T.A., 2013. Deep-ocean mineral deposits as a source of critical
505 metals for high- and green-technology applications: comparison with land-based resources. Ore Geol. Rev., 51, 1–14.
506 http://dx.doi.org/10.1016/j.oregeorev.2012.12.001.

507 Hein, J.R., Yeh, H.W., Gunn, S.H., Sliter, W.V., Benninger, L.M., Wang, C.H., 1993. Two Major Cenozoic Episodes
508 of Phosphogenesis Recorded in Equatorial Pacific Seamount Deposits. Paleoceanography, 8, 293–311.

509 Hyeong, K., Kim, J., Yoo, C.M., Moon J.-W., Seo, I., 2013. Cenozoic history of phosphogenesis recorded in the
510 ferromanganese crusts of central and western Pacific seamounts: Implications for deepwater circulation and
511 phosphorus budgets. Palaeogeogr. Palaeoclimatol. Palaeoecol., 392, 293–301.

512 Josso, P., Parkinson, I. Horstwood, M., Lusty, P., Chenery, S., Murton, B., 2019. Improving confidence in
513 ferromanganese crust age models: A composite geochemical approach. Chemical Geology, 513, 108-119.

514 Kashiwabara, T., Oishi, Y., Sakaguchi, A., Sugiyama, T., Usui, A., Takahashi, Y., 2014. Chemical processes for the
515 extreme enrichment of tellurium into marine ferromanganese oxides. Geochimica et Cosmochimica Acta, 131, 150-
516 163.

517 Kennett, J.P., 1977. Cenozoic evolution of Antarctic glaciation, the circum-Antarctic Ocean, and their impact on
518 global paleoceanography. Journal of Geophysical Research: Oceans and Atmospheres, 82(27): 3843–3860.
519 https://doi.org/10.1029/JC082i027p03843

520 Kennett, J.P., Srinivasan, M.S., 1983. Neogene Planktonic Foraminifera: A Phylogenetic Atlas. Stroudsburg, PA
521 (Hutchinson Ross).

522 Koschinsky A., Halbach P., 1995. Sequential leaching of marine ferromanganese precipitates: genetic implications.
523 Geochimica et Cosmochimica Acta, 59, 5113-5132.

524 Koschinsky A., Halbach P., Hein, J.R., Mangini, A., 1996. Ferromanganese crusts as indicators for
525 paleoceanographic events in the NE Atlantic. Geol. Runsch., 85, 567-576.

526 Koschinsky A., Stascheit A., Bau M., Halbach P., 1997. Effects of phosphatization on the geochemical and
527 mineralogical composition of marine ferromanganese crusts. Geochimica et Cosmochimica Acta, 61, 4079–4094.

528 Koschinsky, A., Bau, M., Marbler, H., Schmidt, K., 2010. Rare valuable metals in marine ferromanganese nodules –
529 contents and accumulation processes. Zeitschrift für Angewandte Geologie, 51 (2), 33-39.

530 Lacasse, C.M., Santos, R.V., Dantas, E.L., Vigneron, Q., de Sousa, I.M.C., Harlamov, V., Lisniowski, M.A.,
531 Pessanha, I.B.M., Frazão, E.P., Cavalcanti, J.A.D., 2017. ^{87}Sr/^{86}Sr dating and preliminary interpretation of magnetic
532 susceptibility logs of giant piston cores from the Rio Grande Rise in the South Atlantic. J. S. Am. Earth Sci., 80, 244–
533 254.

534 Ling, H.F., Burton, K.W., O'Nions, R.K., Kamber, B.S., von Blanckenburg, F., Gibb, A.J., Hein, J.R., 1997.
535 Evolution of Nd and Pb isotopes in central Pacific sea water from ferromanganese crusts. Earth and Planetary Science
536 Letters, 146(1-2), 1-12.

537 Loeblich, A.R., Tappan, H. Foraminiferal Genera and their Classification., 1987. Van Nostrand Reinhold Company,
538 New York. 970pp.

539 Manceau, A., Lanson, M., Takahashi, Y., 2014. Mineralogy and crystal chemistry of Mn, Fe, Co, Ni and Cu in a
540 deep-sea Pacific polymetallic nodule. Am. Mineral., 99, 2068-2083.

541 Manheim, F. T., Lane-Bostwick, C. M., 1989. Chemical composition of ferromanganese crusts in the world ocean: a
542 review and comprehensive database, U.S. Geological Survey Open File Report 89-020, 200 pp.,

543 Marino, E., González, F.J., Somoza, L., Lunar, R., Ortega, L., Vázquez, J.T., Reyes, J., Bellido, E., 2017. Strategic
544 and rare elements in Cretaceous-Cenozoic cobalt-rich ferromanganese crusts from seamounts in the Canary Island
545 Seamount Province (northeastern tropical Atlantic). Ore Geol. Rev., 87, 41–61. Available at:
546 http://dx.doi.org/10.1016/j.oregeorev.2016.10.005.

547 McLennan, S.M., 1989. Rare earth elements in sedimentary rocks; influence of provenance and sedimentary
548 processes. Reviews in Mineralogy and Geochemistry, 21(1), 169–200.

549 Mohriak, W., Nóbrega, M., Odegard, M.E., Gomes, B.S. Dickson, W.G., 2010. Geological and geophysical
550 interpretation of the Rio Grande Rise, south-eastern Brazilian margin: Extensional tectonics and rifting of continental
551 and oceanic crusts. Petrol. Geosci., 16, 231–245.

552 Nozaki, T., Takaya, Y., Toyofuku, T., Tokumaru, A., Goto, K.T., Chang, Q., Kimura, J.I., Kato, Y., Suzuki, K.,
553 Augustin, A.H., Kitazato, H., 2017. Depositional Age of a Fossil Whale Bone from São Paulo Ridge, South Atlantic
554 Ocean, Based on Os Isotope Stratigraphy of a Ferromanganese Crust. Resour. Geol., 67, 442–450.

555 Peacock, C.L., Sherman, D.M., 2007. Crystal chemistry of Ni in marine ferromanganese crusts and nodules.
556 American Mineralogist, 92, 1087-1092.

557 Piepgras, D.J., Wasserburg, G.J., 1987. Rare earth element transport in the western North Atlantic inferred from Nd
558 isotope observations, Geochimica et Cosmochimica Acta, 51, 1257–1271.

559 Puteanus, D., Halbach, P., 1988. Correlation of Co concentration and growth rate — a method for age determination
560 of ferromanganese crusts. Chemical Geology, 69 (1–2), 73–85. http://dx.doi.org/10.1016/0009-2541(88)90159-3.

561 Reynolds, B.C., Frank, M., O'Nions, R.K., 1999. Nd- and Pb-isotope time series from Atlantic ferromanganese
562 crusts: implications for changes in provenance and paleocirculation over the last 8 Myr. Earth Planet. Sci. Lett. 173,
563 381-396.

564 Rickli J., Frank M., Halliday A.N., 2009. The hafnium–neodymium isotopic composition of Atlantic seawater. Earth
565 Planet. Sci. Lett., 280, 118–127.

566 Rohde, J.K., van den Bogaard, P., Hoernle, K., Hauff, F., Wener, R., 2013. Evidence for an age progression along the
567 Tristan-Gough volcanic track from new $^{40}Ar/^{39}Ar$ ages on phenocryst phases. Tectonophysics, 604, 60-71.

568 Rutgers v.d. Loeff, M., Geibert, W., 2008. U- and Th-Series Nuclides as Tracers of Particle Dynamics, Scavenging
569 and Biogeochemical Cycles in the Oceans. In: Krishnaswami, S., Kirk Cochran, J. (Eds.), Radioactivity in the
570 environment. Elsevier, Amsterdam, pp. 227-268.

571 Schmidt, K., Bau, M., Hein, J.R., Koschinsky, A., 2014. Fractionation of the geochemical twins Zr-Hf and Nb-Ta
572 during scavenging from seawater by hydrogenetic ferromanganese crusts. Geochimica et Cosmochimica Acta, 140,
573 468–487. Available at: http://dx.doi.org/10.1016/j.gca.2014.05.036.

574 Stichel, T., Frank, M., Rickli, J., Haley, B.A., 2012. The hafnium and neodymium isotope composition of seawater in
575 the Atlantic sector of the Southern Ocean. Earth Planet. Sci. Lett., 317–318, 282–294.

576 Thompson, G., Humphris, S. E., Schilling, J., 1983. Petrology and geochemistry of basaltic rocks from Rio Grande
577 Rise, South Atlantic; Deep Sea Drilling Project Leg 72, Hole 516F. Initial Reports of the Deep Sea Drilling Project,
578 Vol. 72, p.457-466. doi:10.2973/dsdp.proc.72.115.1983

579 Uspenskaya, T.Y., Gorshkov, A.I., Sivtsov, A. V., 1987. Mineralogy and Internal Structure of Fe-Mn Nodules from
580 the Clarion-Clipperton Fracture Zone. Int. Geol. Rev., 29(3), 363–371.

581 Wedepohl, K.H., 1995. The composition of the continental-crust. Geochimica et Cosmochimica Acta, 59(7), 1217–
582 1232.
583
584 Wegorzewski, A.V., Kuhn, T., Dohrmann, R., Wirth, R., Grangeon, S., 2015. Mineralogical characterization of
585 individual growth structures of Mn-nodules with diferente Ni+Cu content from the central Pacific Ocean. Am.
586 Mineral., 100, 2497-2508.

587 Wegorzewski, A.V., Kuhn, T., 2014. The influence of suboxic diagenesis on the formation of manganese nodules in
588 Clarion Clipperton nodule belt of the Pacific Ocean. Mar. Geol., 357, 123-138.

589 Wegorzewski, A.V., Grangeron, S., Webb, S.M., Heller, C., Kuhn, T., 2010. Mineralogical transformations in
590 polymetallic nodules and the charge of Ni, Cu and Co crystal-chemistry upon burial in sediments. Geochimica et
591 Cosmochimica Acta, 282, 19-37.

592 Yi, L., Medina-Elizalde, M., Kletetschka, G., Yao, H., Simon, Q., Paterson, G., Bourlès, D., Deng, X., Du, J., Qin,
593 H., Chen, Y., Xie, Q., Xiao, J., Wang, Y., Andreucci, C., Keddadouche, K., Aumaître, G., Liu, Y., Wang, H., Zhu,
594 R., 2020. The potential of marine ferromanganese nodules from Eastern Pacific as recorders of Earth's magnetic field

595   changes during the past 4.7 Myr: a geochronological study by magnetic scanning and authigenic 10Be/9Be dating.

596   Journal of Geophysical Research: Solid Earth. 10.1029/2019JB018639.

597

598

599 **TABLES**

600 Table 1: Coordinates and water depth from dredging stations.

Dredging Station	Leg	Sample prefix	Initial depth (m)	Final depth (m)	Initial Latitude (S)	Initial Longitude (W)	Final Latitude (S)	Final Longitude (W)
					Dredging initial and final coordinates			
ERG 064	1	ML64	1105	995	30.811120	35.172832	30.820700	35.178700
ERG 039	1	ML39	830	800	31.148266	35.223911	31.159890	35.214233
ERG 011	1	ML11	990	950	30.495476	36.302307	30.486013	36.302361
ERG 067	1	ML67	1000	950	31.045689	35.711288	31.048300	35.710900
ERG 075	1	ML75	1440	1376	30.318943	36.479797	30.332474	36.485876
ERG 077	1	ML77	1542	1200	30.096700	36.827300	30.104900	36.827600
ERG 025	2	DC25	702	1088	30.419412	36.456264	30.700154	36.016902
ERG 005	2	DC05	1225	1345	30.558989	36.116371	30.335410	36.073223
ERG 010	2	DC10	1740	1640	30.955885	35.020271	30.946175	35.038647
ERG 038	2	DC38	1798	1700	32.099903	32.641815	32.099880	32.662918
ERG 039	2	DC39	1240	1150	32.099991	32.662758	32.099967	32.664719
ERG 061	2	DC61	1245	1165	33.524723	31.096963	33.536652	31.096920
ERG145	4	HS145	688	850	29.800217	36.404784	29.785855	36.395339

601

602 Table 2: Sample characteristics and mineralogical composition.

Samples	Subsample	Substrate	Macroscopic morphology	Total thickness (mm)	Powdered thickness (mm)[a]	Mineralogy
DC05A	-	Phosphorite	Nodule, Massive, phosphatized	30	0-30	10Å stable Mn-phase, CFA
DC10C	-	Phosphorite	Laminated/botryoidal	40	0-40	Vernadite (δ-MnO$_2$)
DC10D	-	Phosphorite	Laminated/botryoidal	50	0-40	Vernadite (δ-MnO$_2$)
DC25A	-	Phosphorite	Massive, phosphatized	25	0-25	10Å stable Mn-phase, CFA
DC25C	-	Phosphorite	Laminated	20	0-20	Vernadite (δ-MnO$_2$)
DC38A	-	Phosphorite	Laminated/botryoidal	25	0-25	Vernadite (δ-MnO$_2$)
DC38B	-	Phosphorite	Botryoidal	25	0-25	Vernadite (δ-MnO$_2$)
DC39B	-	Phosphorite	Botryoidal	10	0-10	Vernadite (δ-MnO$_2$)
DC61B	-	Volcanic	Laminated	12	0-12	Vernadite (δ-MnO$_2$)
ML39B	-	Phosphorite	Layered, phosphatized	18	0-18	10Å stable Mn-phase, CFA
ML64B	-	Phosphorite	Layered	20	0-20	Vernadite (δ-MnO$_2$)
ML67B	2	Older crust	Layered	36	0-6	n.d.
	1	-	Massive		6-36	10Å stable Mn-phase, CFA
ML75A	-	Phosphorite	Laminated/botryoidal	25	0-25	Vernadite (δ-MnO$_2$)
ML77A	-	Phosphorite	Laminated	16	0-16	Vernadite (δ-MnO$_2$)
HS145A[b]	-	Phosphorite	Botryoidal	30	-	n.d.
ML11A[b]	-	Older crust	Layered	35	-	n.d.

603 [a]Powdered thickness is measured from the top of the sample to the bottom; [b]Samples analyzed for [87]Sr/[86]Sr ratio; n.d.:

604 not determined;

605

606 Table 3: WDS (Wavelength-Dispersive X-Ray Spectroscopy) results of EPMA of layered growth

607 structures of different reflectivity (low reflectivity = dark) and (higher reflectivity = light) within sample

608 ML77A.

Dark Layers							Light Layers						
Mn wt.%	Fe wt.%	Ni wt.%	Zn wt.%	Co wt.%	Cu wt.%	Total wt.%	Mn wt.%	Fe wt.%	Ni wt.%	Zn wt.%	Co wt.%	Cu wt.%	Total wt.%
18.79	11.60	0.35	0.14	0.20	0.00	31.08	14.40	19.07	0.23	0.11	0.18	0.07	34.06

17.97	11.81	0.32	0.05	0.18	0.00	30.33	15.38	18.64	0.23	0.08	0.17	0.00	34.50
17.24	12.44	0.24	0.22	0.04	0.08	30.25	16.26	14.87	0.31	0.16	0.48	0.09	32.16
16.59	13.20	0.37	0.20	0.14	0.06	30.57	16.16	14.78	0.19	0.22	0.40	0.00	31.75
17.52	13.29	0.22	0.14	0.13	0.08	31.38	16.00	16.42	0.23	0.27	0.38	0.00	33.29
15.98	14.30	0.27	0.10	0.09	0.08	30.83	12.97	17.56	0.15	0.21	0.35	0.04	31.28
15.52	14.62	0.26	0.31	0.14	0.03	30.89	15.10	17.34	0.26	0.01	0.37	0.01	33.09
16.38	13.78	0.30	0.07	0.19	0.00	30.71	12.26	17.65	0.18	0.96	0.36	0.00	31.40
15.63	13.74	0.28	0.05	0.24	0.11	30.06	19.30	11.90	0.35	0.13	0.37	0.03	32.09
17.03	12.55	0.26	0.00	0.27	0.06	30.18	16.47	13.73	0.25	0.15	0.41	0.00	31.01
17.46	11.16	0.30	0.15	0.20	0.00	29.27	16.77	14.36	0.26	0.17	0.23	0.00	31.77
16.91	11.39	0.26	0.08	0.25	0.00	28.89	16.15	16.79	0.23	0.26	0.31	0.00	33.74
18.58	11.81	0.28	0.08	0.20	0.00	30.95	15.36	17.93	0.17	0.16	0.14	0.00	33.75
18.73	11.71	0.35	0.06	0.29	0.00	31.15	18.24	12.98	0.25	0.16	0.42	0.00	32.05
19.33	11.51	0.32	0.11	0.33	0.02	31.62	17.46	12.54	0.24	0.17	0.36	0.01	30.78
18.66	10.85	0.27	0.14	0.26	0.00	30.17	17.86	12.15	0.23	0.00	0.51	0.04	30.78
18.18	11.23	0.27	0.12	0.27	0.10	30.16	14.35	17.22	0.14	0.21	0.30	0.09	32.31
18.22	10.50	0.38	0.15	0.50	0.00	29.76	17.74	12.76	0.24	0.22	0.51	0.08	31.56
17.72	10.48	0.32	0.02	0.39	0.03	28.97	18.33	12.24	0.27	0.11	0.29	0.01	31.24
17.67	10.56	0.28	0.07	0.34	0.00	28.92	16.71	12.41	0.35	0.32	0.41	0.08	30.27
18.26	11.66	0.33	0.15	0.45	0.05	30.89	17.72	12.74	0.32	0.33	0.53	0.06	31.71
18.43	11.41	0.28	0.15	0.39	0.05	30.70	17.96	12.20	0.34	0.26	0.33	0.03	31.12
17.01	10.73	0.28	0.08	0.54	0.00	28.64	17.25	12.64	0.32	0.61	0.41	0.00	31.22
18.58	11.01	0.36	0.22	0.48	0.07	30.72	14.98	16.85	0.21	0.36	0.31	0.05	32.77
17.79	10.27	0.33	0.17	0.46	0.00	29.01	17.99	11.39	0.26	0.25	0.40	0.00	30.28
17.84	10.94	0.26	0.13	0.40	0.10	29.67	18.60	13.11	0.26	0.27	0.43	0.04	32.71
16.98	10.02	0.29	0.16	0.30	0.08	27.83	17.45	14.39	0.27	0.33	0.30	0.03	32.78
18.47	10.90	0.29	0.27	0.49	0.04	30.47	16.31	14.69	0.20	0.19	0.27	0.10	31.76
16.58	12.26	0.29	0.39	0.49	0.14	30.14	19.09	12.24	0.30	0.19	0.53	0.00	32.34
15.05	14.18	0.22	0.30	0.24	0.00	29.99	15.45	17.61	0.21	0.14	0.36	0.00	33.77
16.48	14.91	0.22	0.30	0.29	0.08	32.28	15.80	15.54	0.25	0.06	0.42	0.00	32.08
16.41	12.49	0.23	0.34	0.33	0.00	29.80	18.59	13.24	0.29	0.27	0.52	0.03	32.94
15.02	12.02	0.24	0.49	0.44	0.05	28.27	15.40	17.94	0.24	0.19	0.16	0.07	34.00
Average	17.36	11.98	0.29	0.16	0.30	0.04	30.14	16.54	14.78	0.25	0.23	0.36	0.03	32.19

609

610

611 Table 4: Foraminifera used for biostratigraphy of phosphorite samples.

Foraminifera	First Occurence	Last Occurence	Reference
Nummulites sp.	Middle Paleocene	Oligocene	Loeblich & Tappan (1987), BouDagher-Fadel (2008)
Discocyclina sp.	Middle Paleocene	Upper Eocene	Loeblich & Tappan (1987), BouDagher-Fadel (2008)
Morozovella sp.	Paleocene	Middle Eocene	Blow (1979)
Orbulina sp.	Middle Miocene (15.1 Ma)	living species	Kennett & Srinivasan (1983)

612

613 Table 5: Electron probe microanalyses (WDS) in samples ML77A, DC38A, DC25A and DC61B. Points

614 of analyses are shown in figures 4 and 5.

Sample	ML77A	ML77A	DC38A	DC25A	DC61B
Spot	EPMA1	EPMA2	EPMA3	EPMA4	EPMA5
Fe (%)	10.63	0.03	1.34	5.39	12.83
Mn	0.12	0.02	0.06	4.07	0.23
P	11.43	0.06	8.51	8.03	2.05
Ca	25.74	36.37	29.95	28.17	6.05
Na	0.87	0.04	0.71	0.67	0.19
Mg	0.55	0.58	0.56	0.66	1.79
F	4.84	0.00	4.82	4.75	0.41
Al	0.44	0.10	1.71	0.53	5.97
Si	0.29	0.18	3.92	0.26	12.13
K	0.02	0.05	0.71	0.07	2.47
Si	1.07	1.07	0.00	0.03	0.01
Ti	0.00	0.00	0.17	0.00	2.37
Cr	0.00	0.00	0.00	0.03	0.06
Co	0.00	0.02	0.02	0.03	0.00
Cu	0.00	0.01	0.06	0.00	0.00

25

Ni	0.02	0.00	0.02	0.04	0.02
Ba	0.05	0.01	0.04	0.00	0.24

615

616

617 Table 6: Bulk composition of ferromanganese crusts from the Rio Grande Rise.

	Non-phosphatized samples							
	ML64B	ML67B-2	ML75A	ML77A	DC10C	DC10D	DC25C	DC38A
Fe %	18.35	17.32	19.03	18.73	21.28	21.32	15.76	19.16
Mn	25.87	24.11	24.30	25.04	23.49	23.05	21.04	23.74
Mn/Fe	1.41	1.39	1.28	1.34	1.10	1.08	1.34	1.24
Ca	3.46	2.66	2.76	2.74	2.57	2.54	8.43	2.62
Na	1.53	1.32	1.56	1.53	1.52	1.46	1.15	1.55
Mg	1.37	1.27	1.25	1.22	1.27	1.30	1.60	1.21
Al	0.54	0.60	0.51	0.46	0.88	1.15	0.41	0.84
K	0.36	0.30	0.33	0.33	0.35	0.46	0.23	0.38
P	0.48	0.49	0.51	0.46	0.50	0.47	0.40	0.49
Co mg/kg	9208	7615	9795	10484	7734	7502	6554	8439
Ni	4740	4848	3715	3823	3416	3607	4216	3734
Cu	387	467	323	366	398	549	323	378
Zn	566	559	535	571	602	652	439	573
V	1093	1020	1057	1038	1069	1110	960	1003
Mo	716	649	633	658	641	642	514	655
Li	6.12	3.06	3.33	2.43	3.38	7.97	2.29	5.01
Sc	4.42	4.68	5.46	5.63	9.74	8.27	4.49	6.42
Ti	9884	10495	11251	11564	10599	10789	8758	10578
Rb	3.20	1.97	2.76	2.85	3.67	7.49	3.06	4.59
Sr	2039	1907	1967	1971	1881	1849	2162	1829
Y	150	179	191	162	206	146	166	154
Zr	367	418	407	450	494	530	271	460
Nb	75	72	85	88	73	89	81	73
Mo	653	631	624	651	578	541	511	629
Te	86.69	90.72	88.93	95.63	60.50	69.13	91.82	72.25
Ba	1324	1359	1311	1447	1338	1575	1258	1394
La	253.92	254.13	301.60	298.90	313.42	288.44	249.38	275.26
Ce	1560.27	1663.15	1629.58	1929.88	1586.37	1928.73	1425.92	1864.80
Pr	51.37	51.22	60.15	59.36	63.29	59.88	54.56	55.50
Nd	205.40	208.61	246.14	236.89	261.90	241.79	223.46	223.85
Sm	42.56	42.39	49.78	47.99	53.06	49.00	46.27	45.57
Eu	9.85	9.94	11.61	10.99	12.78	11.52	10.65	10.53
Gd	43.02	43.63	51.56	47.58	58.24	48.89	46.59	46.19
Tb	6.57	6.74	7.79	7.36	8.81	7.62	7.12	7.14
Dy	39.80	41.26	47.53	45.05	54.70	45.15	42.53	42.43
Ho	8.09	8.73	9.78	9.17	11.13	9.01	8.55	8.63
Er	23.58	25.42	28.72	26.46	32.01	24.94	24.44	24.35
Tm	3.40	3.72	4.08	3.82	4.45	3.56	3.42	3.54
Yb	20.97	23.56	25.25	23.61	28.67	22.30	20.73	22.30
Lu	3.09	3.63	3.79	3.44	4.27	3.27	3.08	3.32
Hf	6.68	6.99	6.85	8.28	9.46	12.26	4.82	8.51
Ta	1.19	1.40	1.38	1.51	1.33	1.70	1.28	1.34
W	145	128	143	156	130	123	122	136
Pb	2202	2363	2407	2411	2110	1981	1945	2204
Th	29.73	26.42	31.73	39.53	26.25	40.57	25.20	37.54
U	12.52	13.21	13.67	12.97	12.91	11.86	11.98	12.24
Y/Ho	18.48	20.51	19.53	17.68	18.52	16.23	19.37	17.80
Zr/Hf	54.87	59.76	59.38	54.31	52.27	43.20	56.33	53.98
Nb/Ta	63.05	51.67	61.69	57.99	54.50	52.61	62.75	54.62
$Ce_{SN}/Ce_{SN}*$[1]	3.14	3.35	2.78	3.33	2.59	3.38	2.81	3.47
$Y_{SN}/Y_{SN}*$[2]	0.66	0.75	0.71	0.64	0.67	0.58	0.69	0.64
ΣREE	2272	2386	2477	2751	2493	2744	2167	2633
G.R. (mm/Ma)[3]	1.88	2.45	1.73	1.58	2.40	2.51	3.08	2.12
Thickness (mm)	20	6	25	16	40	40	20	25
Age (Ma)	10.6	2.4	14.4	10.1	16.7	15.9	6.5	11.8

618 [1] SN: Shale normalized. $Ce_{SN}/Ce_{SN}* = Ce_{SN}/(0.5La_{SN} + 0.5 Pr_{SN})$

619 [2] SN: Shale normalized. $Y_{SN}/Y_{SN}* = Y_{SN}/(0.5Dy_{SN} + 0.5Ho_{SN})$

620 [3] G.R. is the growth rate calculated as G.R.=1,28/[Co(%)-0,24] (Puteanus & Halbach, 1988)

26

621

622

623

624

625   Table 6: continued.

	Non-phosphatized samples			Phosphatized samples			
	DC38B	DC39B	DC61B	ML39B	ML67B-1	DC05A	DC25A
Fe %	19.91	20.18	17.88	12.71	6.61	9.14	7.96
Mn	20.87	22.97	25.12	19.00	16.09	15.62	10.06
Mn/Fe	1.05	1.14	1.41	1.49	2.43	1.71	1.26
Ca	2.78	2.77	2.83	11.93	18.08	11.54	20.67
Na	1.66	1.63	2.08	1.01	0.93	0.94	0.81
Mg	1.31	1.20	1.41	1.85	1.97	1.94	1.94
Al	1.11	0.59	0.71	1.06	1.24	1.70	1.57
K	0.36	0.34	0.34	0.26	0.27	0.39	0.23
P	0.49	0.56	0.45	1.50	4.70	2.70	5.21
Co mg/kg	9718	9383	10101	4234	2864	5224	2069
Ni	2999	3501	3916	5825	6878	5391	4341
Cu	441	421	286	375	306	716	395
Zn	540	562	546	508	859	596	534
V	877	1055	900	914	502	574	467
Mo	517	601	670	455	314	391	247
Li	3.62	2.12	2.50	37.45	93.73	78.01	66.42
Sc	17.23	6.11	8.74	4.35	6.20	6.23	7.41
Ti	11591	12382	10328	7464	3815	5664	4083
Rb	5.26	3.90	2.43	3.20	5.11	9.95	6.14
Sr	1722	1966	1860	1554	1727	1127	1332
Y	210	201	197	164	234	201	195
Zr	526	483	466	264	172	242	191
Nb	86	108	66	58	29	44	33
Mo	487	598	638	423	290	384	217
Te	76.26	92.10	72.30	65.52	30.45	42.03	24.42
Ba	1145	1338	1061	1200	901	782	571
La	346.17	292.91	321.14	178.55	165.53	137.24	107.72
Ce	1837.02	1904.66	1465.55	1058.96	525.95	641.25	349.56
Pr	73.69	56.80	64.43	36.20	29.47	24.73	20.39
Nd	298.30	232.72	260.41	147.73	126.07	104.02	87.59
Sm	60.78	47.26	52.00	31.01	25.53	21.14	18.16
Eu	14.51	11.05	12.34	7.35	6.21	5.13	4.46
Gd	62.69	49.46	54.79	33.22	30.77	25.22	21.97
Tb	9.74	7.65	8.35	5.00	4.44	3.82	3.28
Dy	57.53	47.12	51.56	30.55	29.60	25.09	21.87
Ho	11.56	9.83	10.62	6.61	6.54	5.64	5.09
Er	32.02	28.87	30.50	18.86	19.48	17.76	15.59
Tm	4.55	4.12	4.31	2.69	2.63	2.55	2.29
Yb	28.47	26.64	27.73	16.46	16.36	16.12	14.40
Lu	4.24	4.02	4.17	2.49	2.49	2.52	2.31
Hf	10.85	9.57	6.87	4.87	3.13	4.47	3.56
Ta	1.89	1.56	1.13	1.09	0.50	0.75	0.53
W	115	134	130	110	63	96	46
Pb	1782	2512	2221	1612	844	1067	547
Th	47.61	37.10	28.69	17.85	9.19	13.75	8.95
U	11.31	14.20	12.32	10.59	9.22	10.03	9.89
Y/Ho	18.12	20.43	18.58	24.84	35.76	35.55	38.38
Zr/Hf	48.51	50.44	67.91	54.15	55.05	54.11	53.62
Nb/Ta	45.40	68.85	58.47	53.21	58.05	58.91	63.36
$Ce_{SN}/Ce_{SN}*$[1]	2.65	3.39	2.34	3.03	1.72	2.52	1.71
$Y_{SN}/Y_{SN}*$[2]	0.65	0.74	0.67	0.92	1.34	1.34	1.48
ΣREE	2841	2723	2368	1576	991	1032	675
G.R. (mm/Ma)[3]	1.75	1.83	1.66	-	-	-	-
Thickness (mm)	25	10	12	-	-	-	-
Age (Ma)	14.3	5.5	7.2	-	-	-	-

626   [1] SN: Shale normalized (Post-Archean Australian Shale, PAAS, of McLennan, 1989). $Ce_{SN}/Ce_{SN}^* = Ce_{SN}/(0.5La_{SN}+0.5\ Pr_{SN})$

627   [2] SN: Shale normalized (Post-Archean Australian Shale, PAAS, of McLennan, 1989). $Y_{SN}/Y_{SN}^* = Y_{SN}/(0.5Dy_{SN}+0.5Ho_{SN})$

628   [3] G.R. is the growth rate calculated as G.R.=1,28/[Co(%)-0,24] (Puteanus & Halbach, 1988)

629   Table 7: $^{87}Sr/^{86}Sr$ results.

Sample	$^{87}Sr/^{86}Sr$ ± 2SE	Age (Ma)
ML11D	0.70860±2	17.6
HS145A	0.70880±2	14.6

630

631

632

633

634

635

636

637

638

639

640

641

642

643

644

645
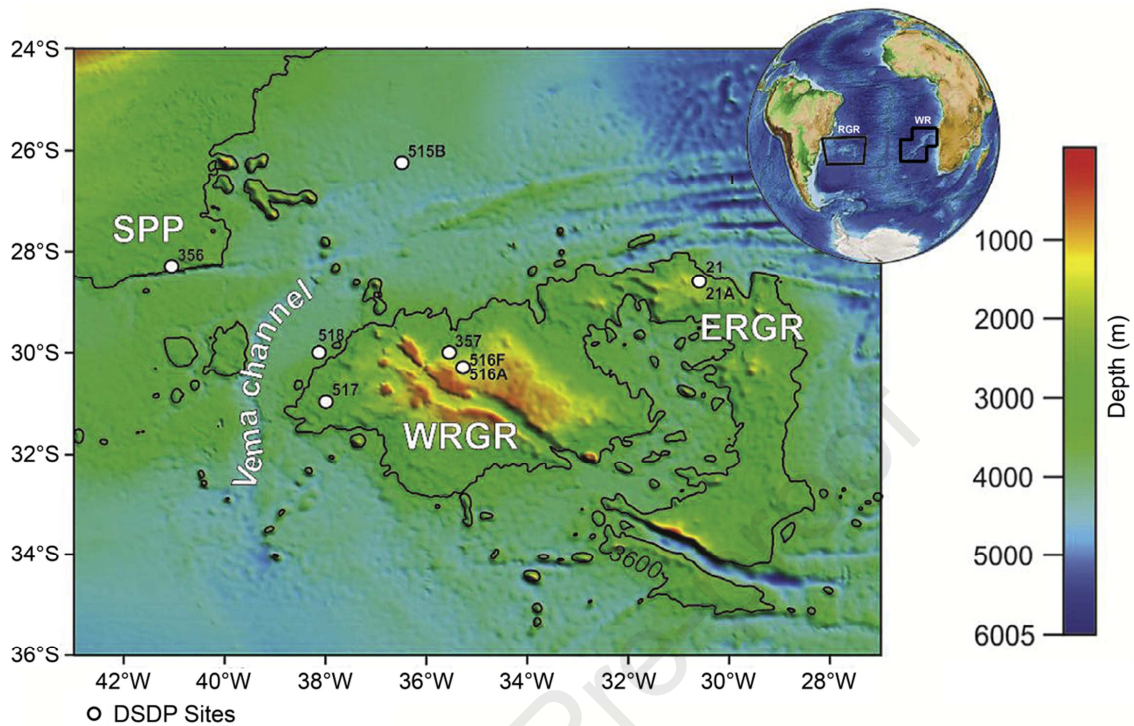
646
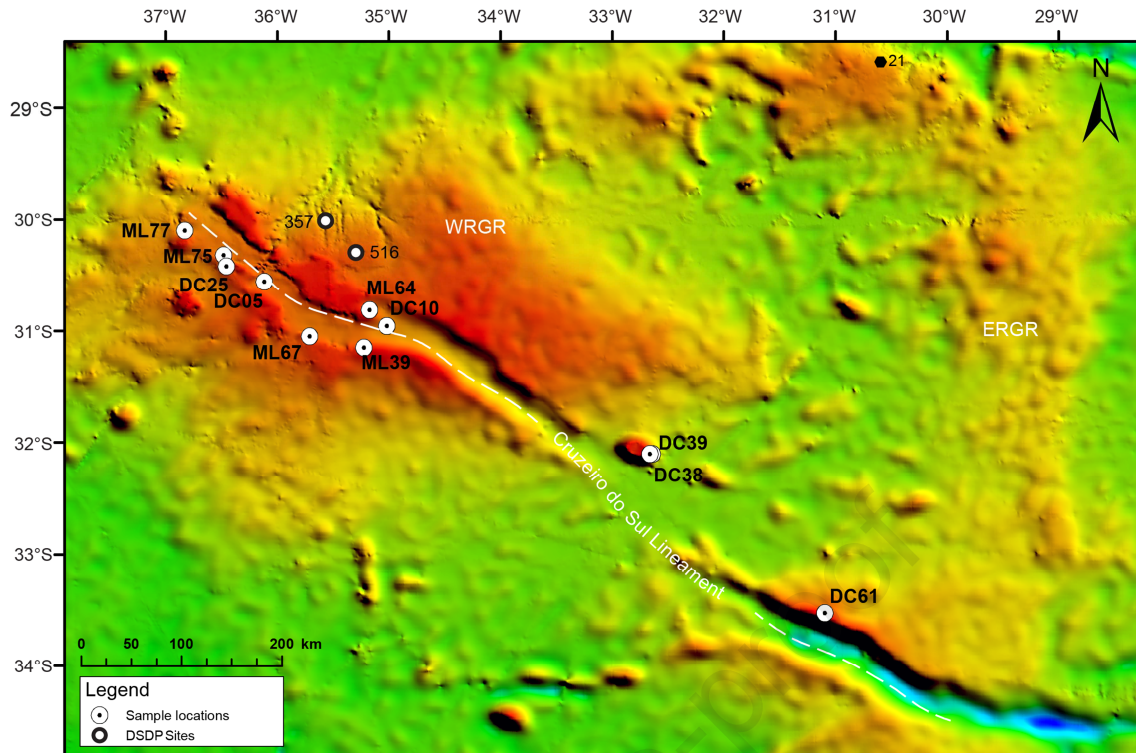
647

648 **FIGURES**

649

650

651 Fig. 1: Bathymetry from ETOPO1 showing West and East Rio Grande Rises (WRGR and ERGR), the

652 Vema channel and the São Paulo Plateau (SPP). White circles are DSDP (Deep Sea Drilling Project) Sites

653 (Constantino et al., 2017). In the globe figure, the position of Walvis Ridge (WR) and Rio Grande Rise

654 (RGR) are shown.

655

656

657 Fig. 2: Sample locations in the Rio Grande Rise. Deep Sea Drilling Project sites 357 and 516 are shown

658 in the map.

659
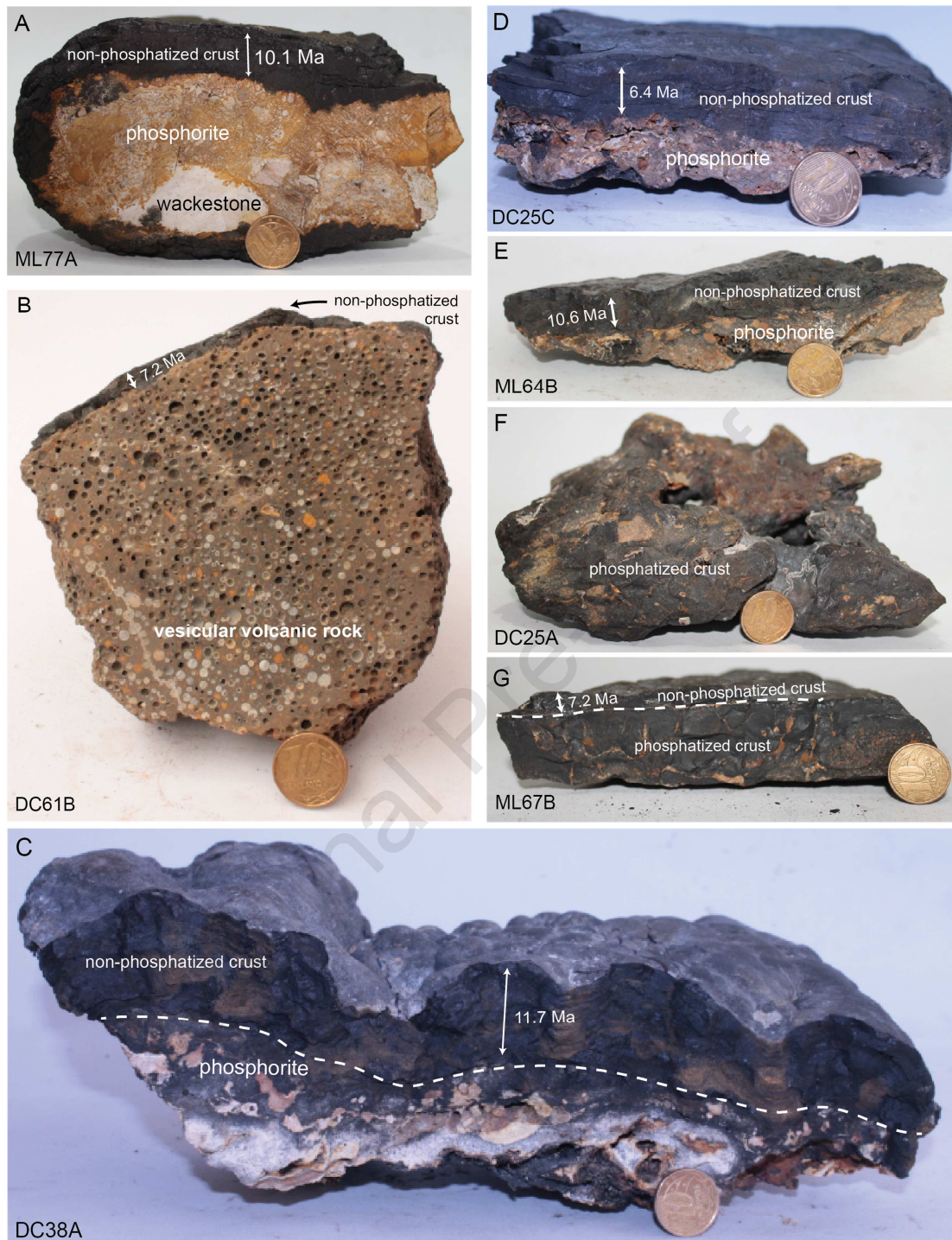
660   Fig. 3: Ferromanganese crust samples from the Cruzeiro do Sul Lineament. Ages shown are minimum

661   estimates based on Co chronology calculations. Coin diameter = 2 cm. A. Sample ML77A. Laminated

662   Fe-Mn crust developed above phosphorite; B. Sample DC61B. Thin Fe-Mn crust above volcanic

663   substrate; C. Sample DC38A. Botryoidal Fe-Mn crust developed above phosphorite. White dashed line

664   indicates the boundary between the pristine crust and the phosphorite substrate impregnated with

665   oxyhydroxides; D. Sample DC25C. Laminated Fe-Mn crust developed above phosphorite; E. Sample

666   ML64B. Laminated crust above phosphorite; F. Sample DC25A. Irregular shaped sample composed of

667   Fe-Mn precipitates in between phosphorites; G. Sample ML67B. 6 mm-thick pristine crust developed

668 above older phosphatized crust. White dashed line indicates the boundary between the old and the new

669 crust generations.

670
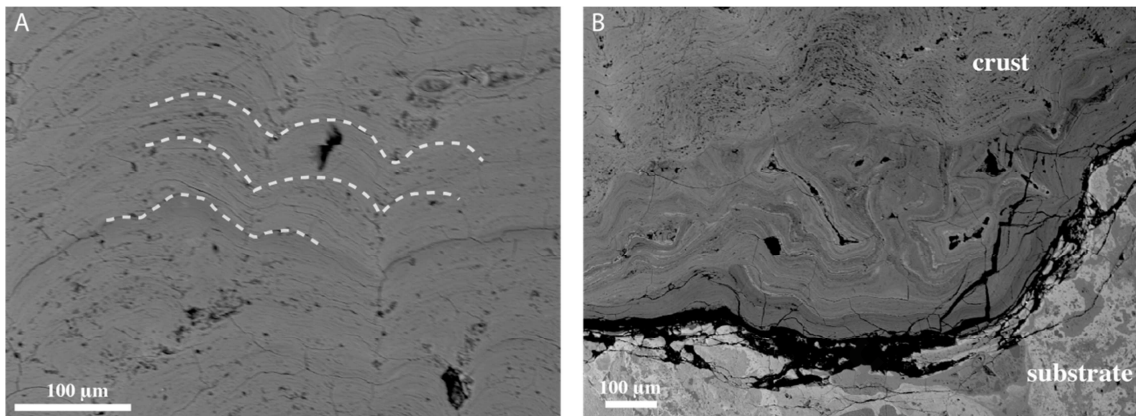
671

672 Fig. 4: Backscattered electrons images of sample ML77A. Layers of higher reflectance present a higher

673 concentration of metals. A. Concave growth structures are shown; B. Contact between the crust and its

674 substrate.

675
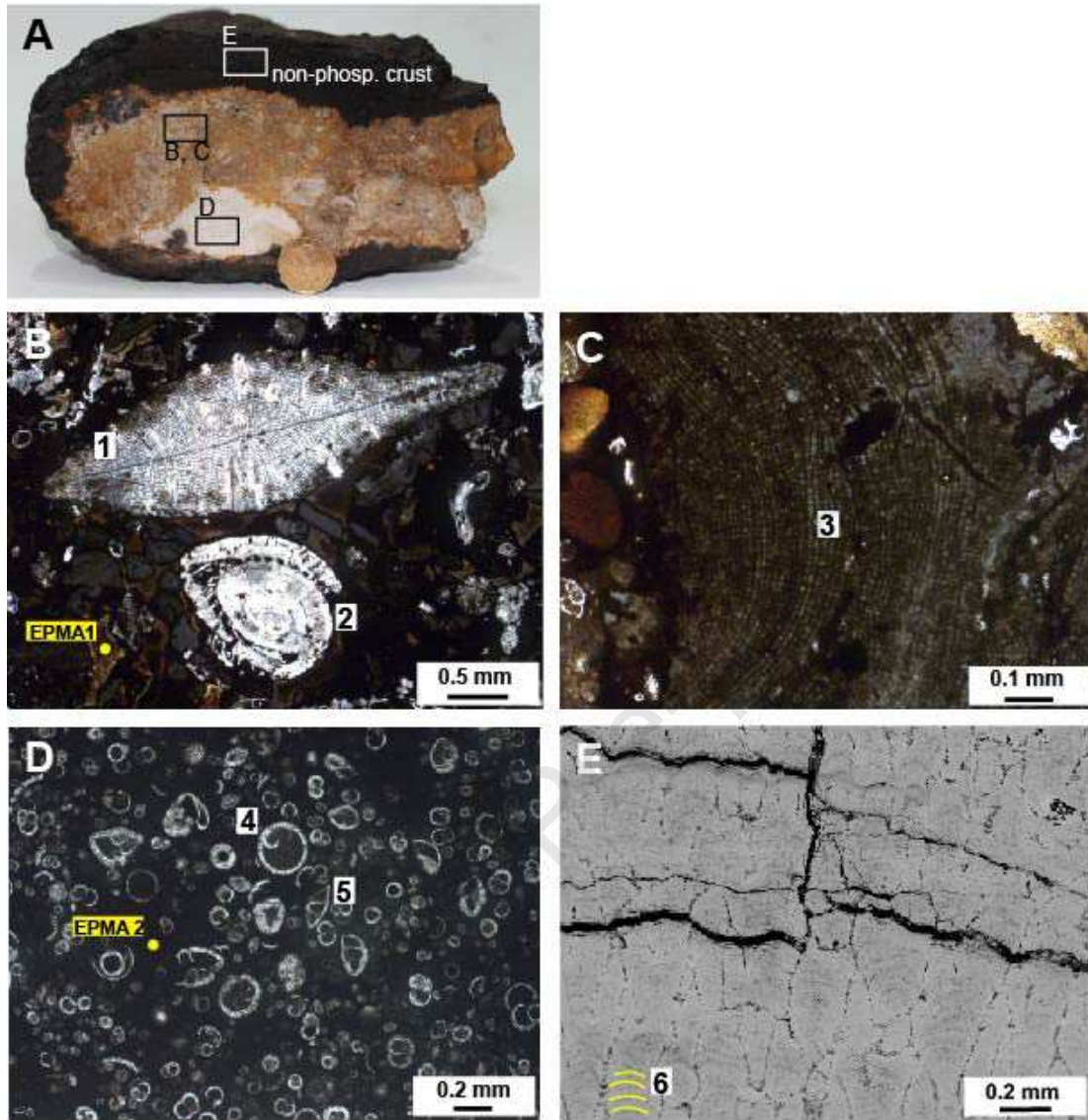
676
677 Fig. 5: A. Sample ML77A. Ferromanganese crust developed above sedimentary rock composed of an
678 Eocene phosphatized packstone (B and C) attached to a Miocene wackestone (D) fragment; B.
679 Photomicrography of Eocene fragment showing *Discocyclina sp.* (1) and *Nummulites sp.* (2) in a
680 carbonate fluorapatite matrix; C. Photomicrography of calcareous structure of Eocene coralline algae (3);
681 D. Photomicrography of Miocene fragment composed of planktic foraminifera in a micritic matrix.
682 *Orbulina sp.* (4) and *Globorotalia sp.* (5) are shown; E. Backscattered electron image of the
683 ferromanganese crust showing layers of different reflectance and concave growth structures (6). Yellow
684 dots are EPMA spot analyses shown in table 4. Coin diameter = 2 cm.
685
686
687
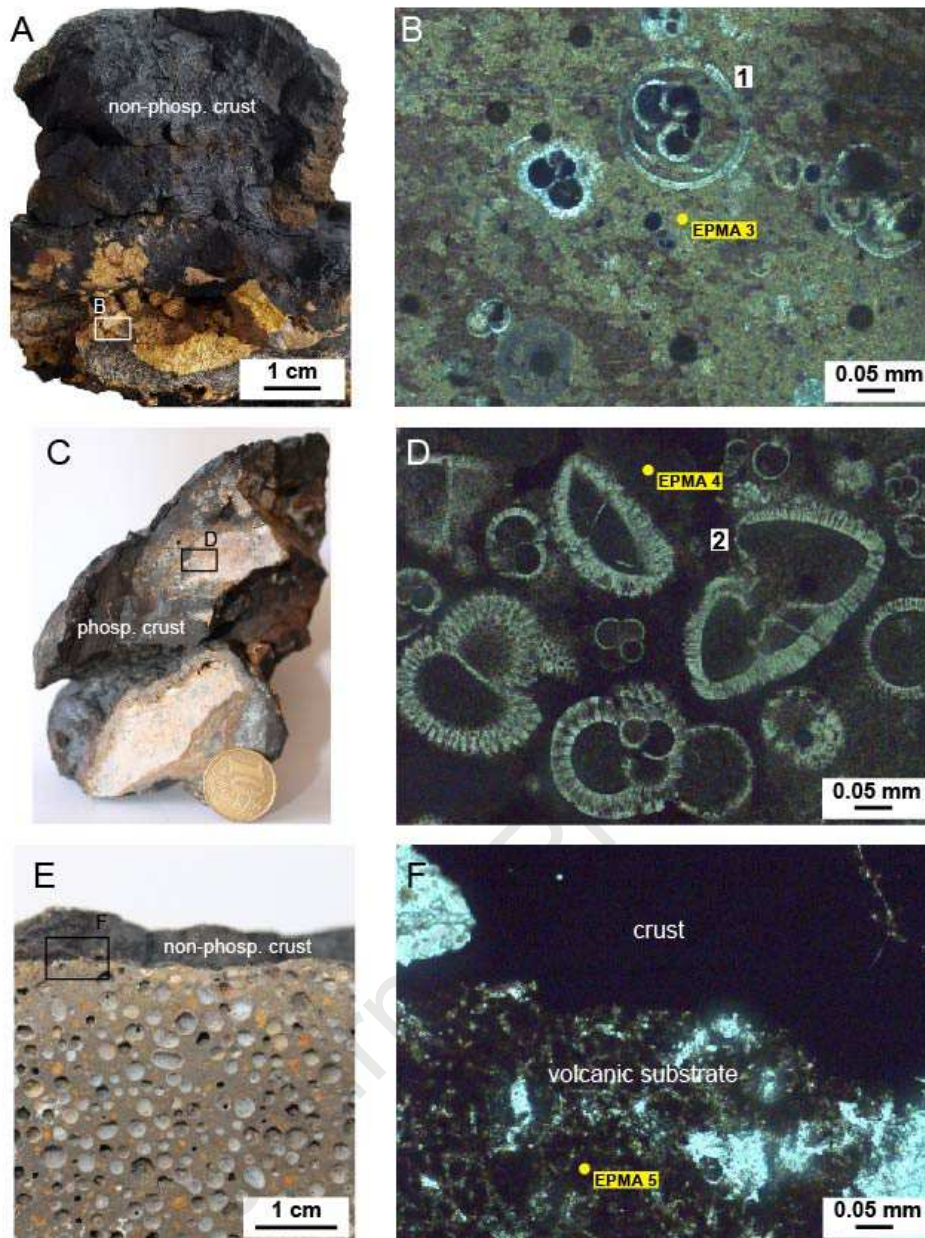
688

689   Fig. 6: A. Sample DC38A; B. Photomicrography of crust substrate in sample DC38A showing *Orbulina*

690   *universa* (1) in a carbonate fluorapatite matrix; C. Sample DC25A; D. Photomicrography of the substrate

691   in sample DC25A showing *Morozovella sp*. in a carbonate fluorapatite matrix; E. Sample DC61B; F.

692   Photomicrography of sample DC61B showing the contact between the volcanic substrate and the

693   overlying ferromanganese crust. Yellow dots are EPMA spot analyses shown in table 4. Coin diameter =

694   2 cm.

695

696
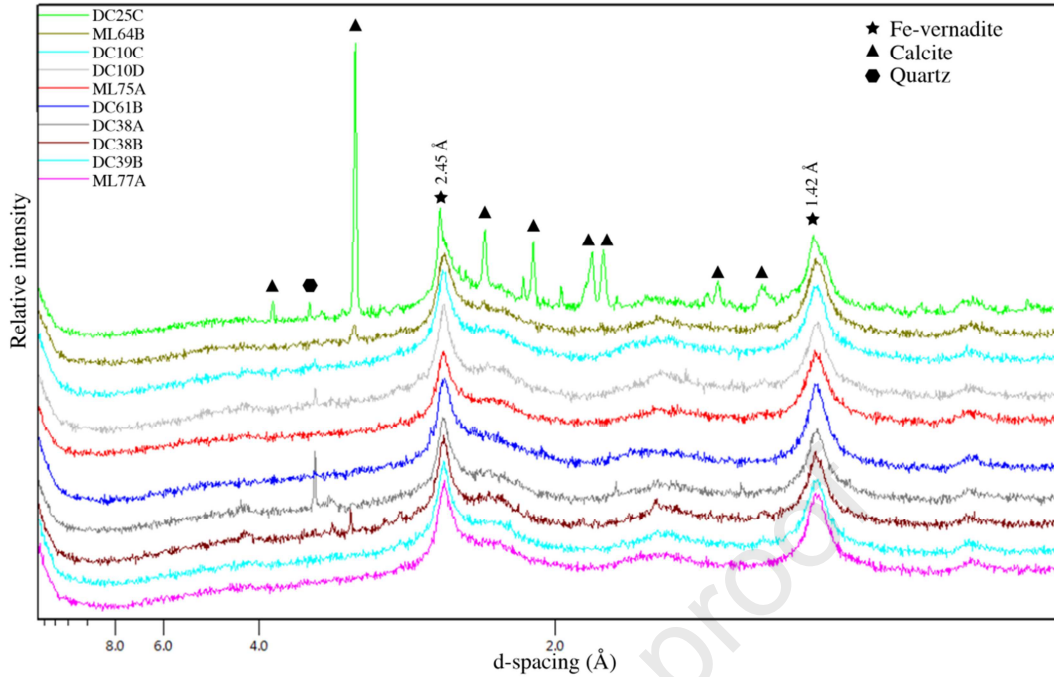
697

698 Fig. 7: XRD patterns of non-phosphatized crust samples. 2.45 and 1.42 Å peaks characterize the Fe-
699 vernadite (δ-MnO_2). Calcite is present in samples DC25C, ML64B and DC38B; quartz is present in
700 samples DC25C, DC10C, DC10D and DC38A.
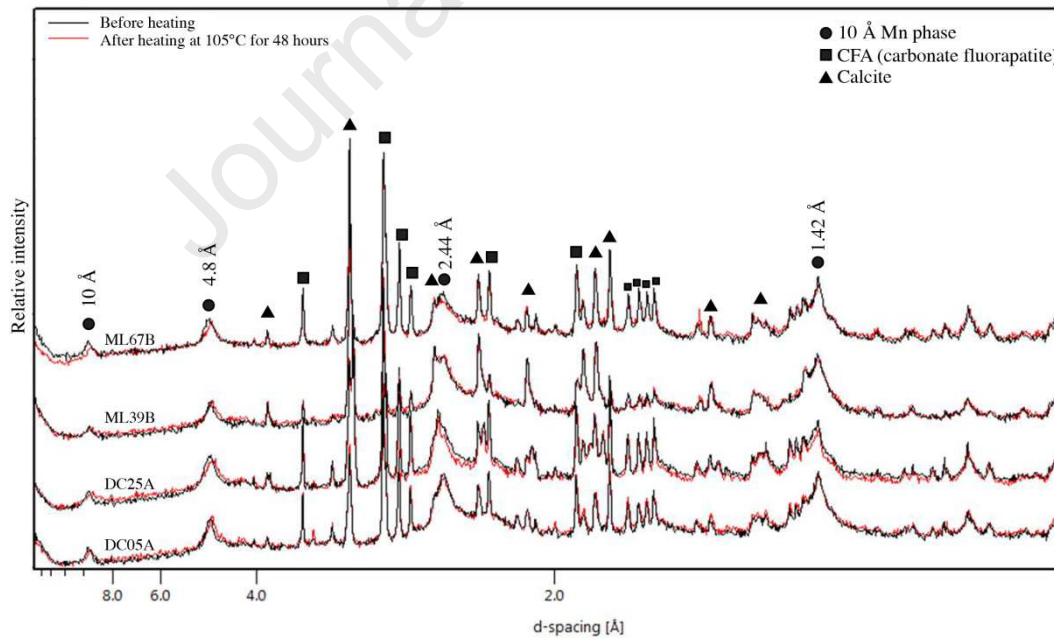
701

702 Fig. 8: XRD patterns of phosphatized crust samples. The 10 Å peak remains present in all samples after
703 heating at 105°C for 48 hours.

704

705

35

706
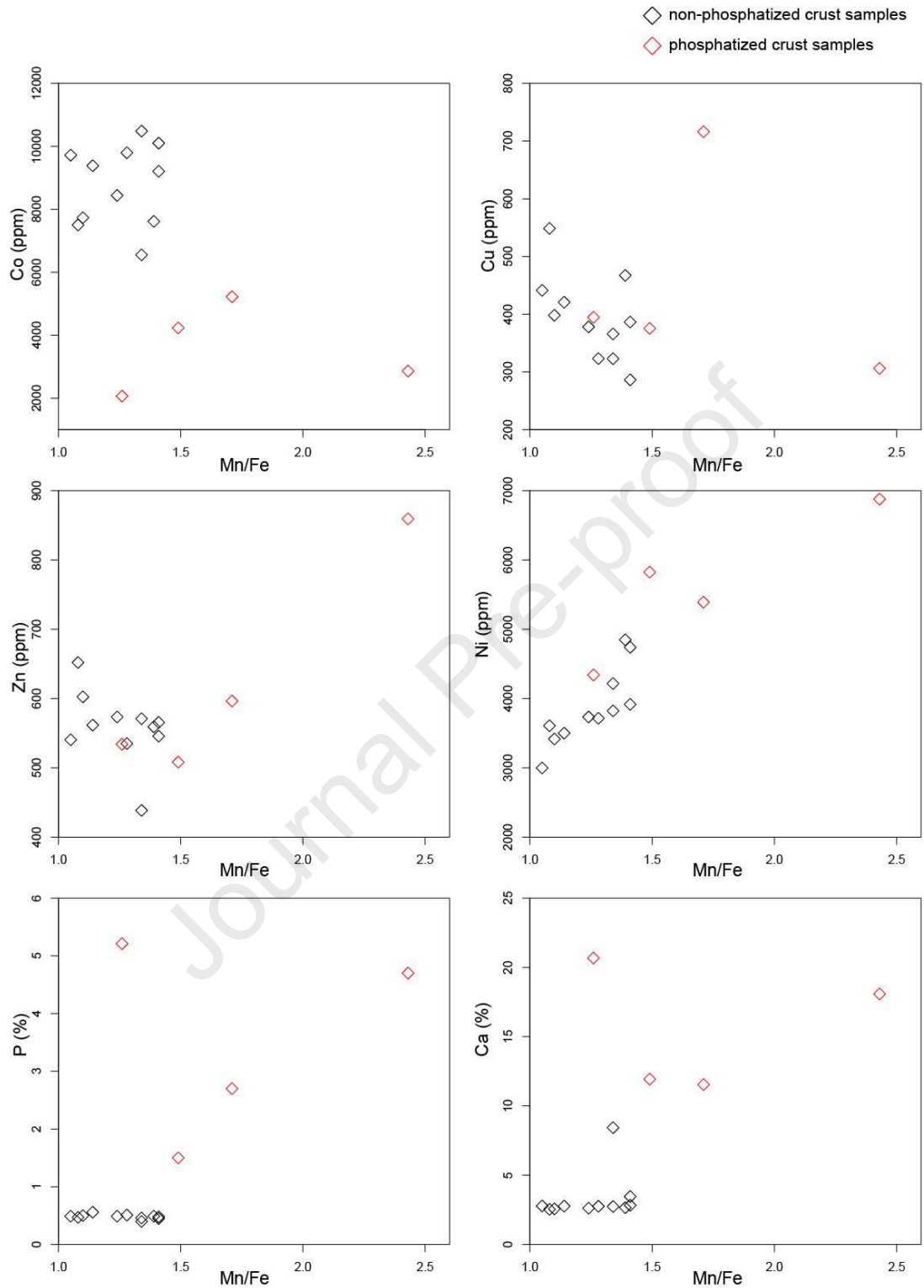
707

708 Fig. 9: Mn/Fe vs elements of crusts from the escarpments of the Rio Grande Rise. Phosphatized crust

709 samples present higher contents of P and Ca.

710
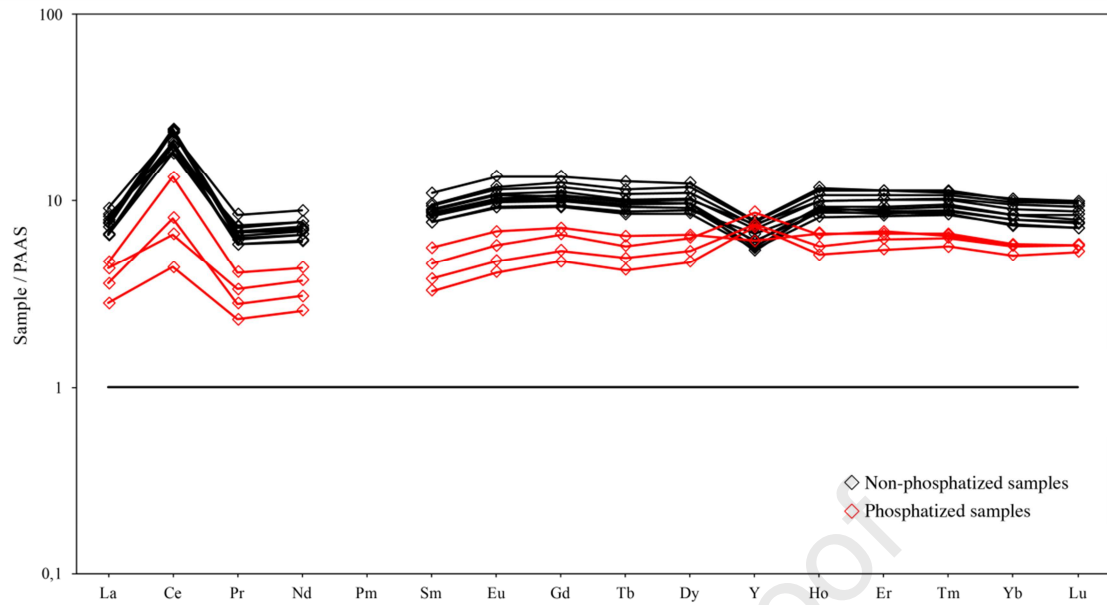
Fig. 10: REY pattern normalized to Post-Archean Australian Shale (PAAS, of McLennan, 1989) of Fe-

Mn crusts from the escarpments of the Rio Grande Rise.

713

714
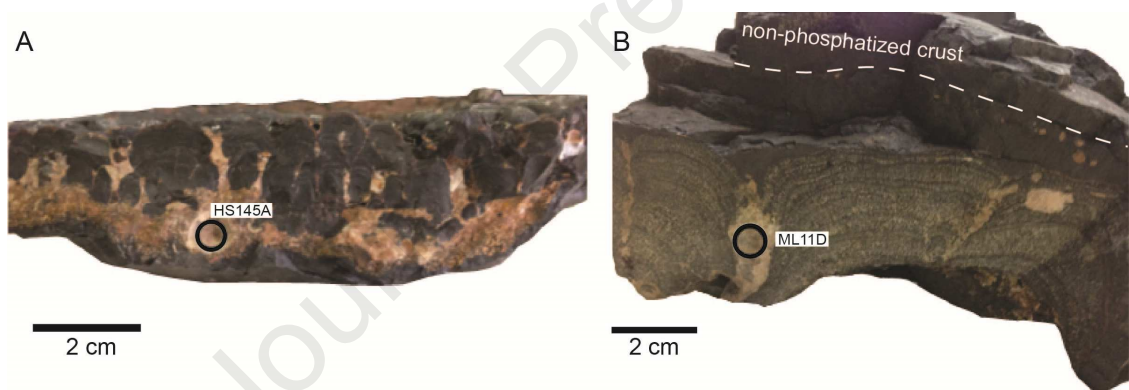
Fig. 11: Sample HS145A (A) and sample MLD11 (B) indicating where ^{87}Sr/^{86}Sr analyses were
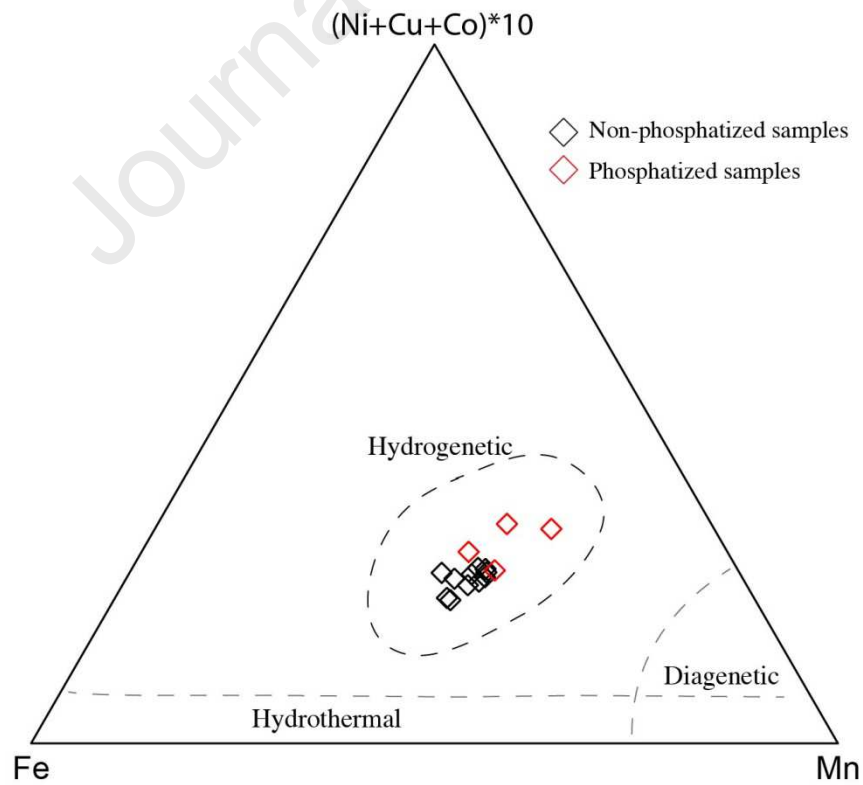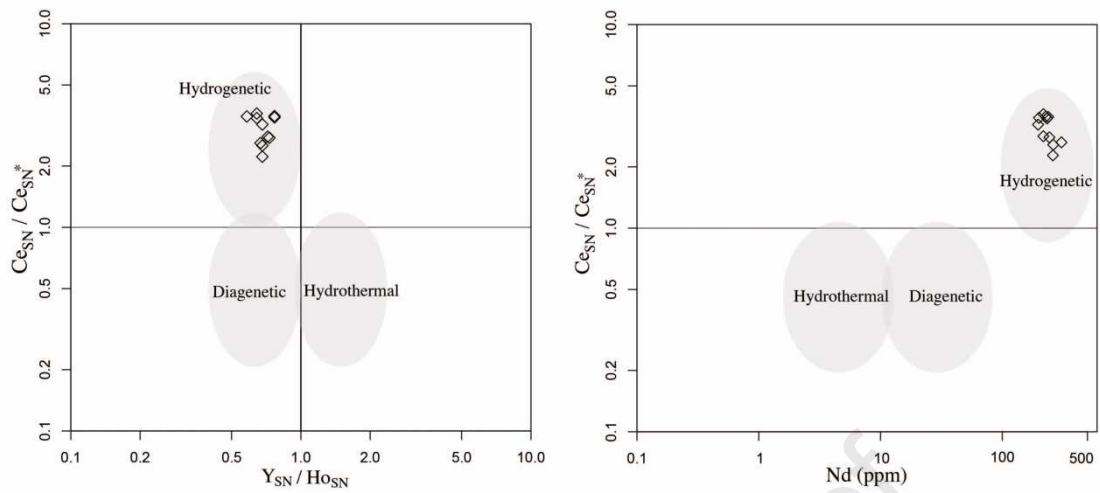
performed.

717

37
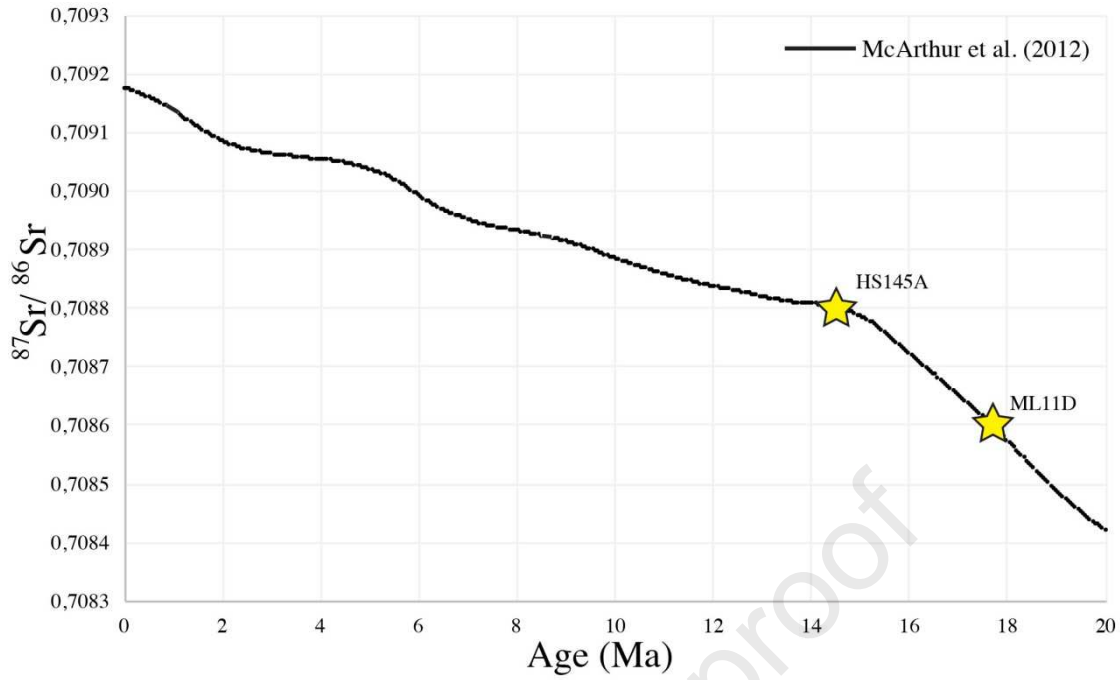
718

719   Fig. 12: Samples HS145a and ML11D plotted in ^{87}Sr/^{86}Sr curve from McArthur et al. (2012) for indirect

720   dating.

721

722

723   Fig. 13: Ternary diagram of Mn, Fe and (Ni+Cu+Co)*10 modified from Bonatti et al. (1972). All

724   analyzed samples plot in the hydrogenetic field.

725

726 Fig. 14: Y_{SN}/Ho_{SN} ratio vs $Ce_{SN}/Ce_{SN}*$, and Nd (ppm) vs $Ce_{SN}/Ce_{SN}*$. SN: shale normalized (PAAS) and

727 $Ce_{SN}*=0.5\ La_{SN} + 0.5\ Pr_{SN}$. The position of the samples indicated by diamond symbols is in the field of

728 hydrogenetic Fe-Mn precipitates. Discriminant diagrams proposed by Bau et al. (2014). Phosphatized

729 samples are not shown because the plot is not appropriate for phosphatized samples.
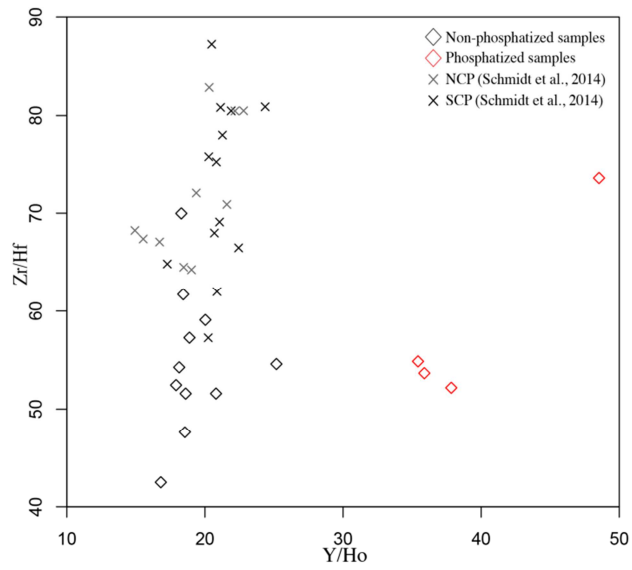
730
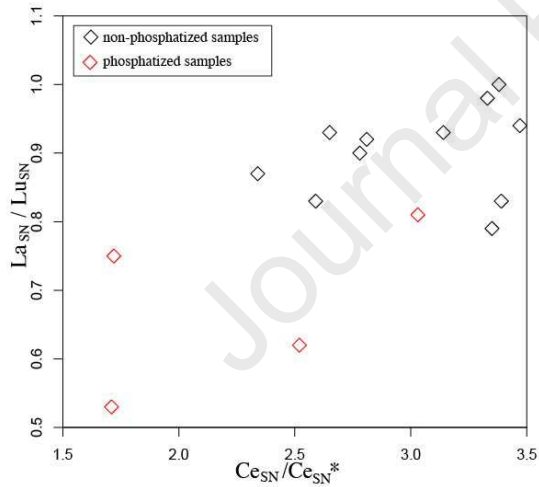
731
732 Fig. 15: $Ce_{SN}/Ce_{SN}*$ vs La_{SN}/Lu_{SN}. Phosphatized samples exhibit lower La_{SN}/Lu_{SN} ratios for having

733 carbonate fluorapatite, that is more enriched in HREE relative to LREE than oxy-hydroxides. $Ce_{SN}/Ce_{SN}*$

734 is also lower in phosphatized samples due to Ce remobilization during phosphatization.

735
736

Fig. 16: Y/Ho vs Zr/Hf plot of samples from the Pacific Ocean (Schmidt et al. 2014) and this study. Zr/Hf ratios are higher in Pacific crusts because they formed in older and more scavenged waters, from which Hf has been removed by particle sorption.

Mineralogy and chemical composition of ferromanganese crusts from the Cruzeiro do Sul Lineament - Rio Grande Rise, South Atlantic

Sousa, I.M.C., Santos, R.V., Koschinsky, A., Bau, M., Wegorzewski, A.V., Cavalcanti, J.A.D., Dantas, E.L.

Highlights:

- Non-phosphatized Fe-Mn crusts in the region developed above Miocene phosphorites.
- Phosphatization was probably caused by a Middle Miocene OMZ expansion in depth.
- Fe-vernadite is the mineral constituent of non-phosphatized Fe-Mn crusts.
- A stable 10 Å-Mn phase is the mineral constituent of phosphatized crusts.
- Estimated age of the crusts is in agreement with data from NE Atlantic.

Declaration of interests

☒ The authors declare that they have no known competing financial interests or personal relationships that could have appeared to influence the work reported in this paper.

☐The authors declare the following financial interests/personal relationships which may be considered as potential competing interests: